

• Original Paper •

Characteristics of the Outer Rainband Stratiform Sector in Numerically Simulated Tropical Cyclones: Lower-Layer Shear versus Upper-Layer Shear

Qi GAO¹, Qingqing LI^{2,3}, and Yufan DAI¹

¹Nanjing University of Information Science and Technology, Nanjing 210044, China

²Key Laboratory of Meteorological Disaster of the Ministry of Education, Nanjing University of Information Science and Technology, Nanjing 210044, China

³State Key Laboratory of Severe Weather, Chinese Academy of Meteorological Sciences, Beijing 100081, China

(Received 25 September 2019; revised 2 January 2020; accepted 22 January 2020)

ABSTRACT

Idealized numerical simulations are conducted in this study to comparatively investigate the characteristics of the stratiform sector in the outer rainbands of tropical cyclones (TCs) in lower- and upper-layer vertical wind shear (VWS) with moderate magnitude. Consistent with the results in previous studies, the outer rainband stratiform sector of the TCs simulated in both experiments is generally located downshear left. Upper-layer VWS tends to produce stronger asymmetric outflow at upper levels in the downshear-left quadrant than lower-layer shear. This stronger asymmetric outflow transports more water vapor radially outward from the inner core to the outer core at upper levels in the downshear-left quadrant in the upper-layer shear experiment. More depositional growth of both graupel and cloud ice thus occurs downshear left in upper layers in the outer core, yielding more diabatic heating and stronger upward motions, particularly in the stratiform-dominated part of the stratiform sector in the upper-layer shear experiment. Resultingly, a better-organized stratiform sector in the outer rainbands is found in the upper-layer VWS experiment than in the lower-layer VWS experiment. The diabatic heating associated with the stratiform sector produces strong midlevel outflow on the radially inward side of, and weak midlevel inflow on the radially outward side of, the heating core, with lower-level inflow beneath the midlevel outflow and upper-level inflow above. The upper-layer VWS tends to produce a deeper asymmetric inflow layer in the outer rainband stratiform sector, with more significant lower-level inflow and tangential jets in the upper-layer VWS experiment.

Key words: stratiform, outer rainband, tropical cyclone, vertical wind shear

Citation: Gao, Q., Q. Q. Li, and Y. F. Dai, 2020: Characteristics of the outer rainband stratiform sector in numerically simulated tropical cyclones: Lower-layer shear versus upper-layer shear. *Adv. Atmos. Sci.*, **37**(4), 399–419, <https://doi.org/10.1007/s00376-020-9202-y>.

Article Highlights:

- Better-organized outer rainband stratiform sectors occur in tropical cyclones in upper-layer shear.
- Moister air related to stronger asymmetric outflow in upper-layer shear favors the downshear-left occurrence of stratiform clouds.
- More significant lower-level inflow and tangential jets are found in the stratiform sector in upper-layer shear.

1. Introduction

Tropical cyclone (TC) spiral rainbands can be classified into inner and outer rainbands based on their locations (Wang, 2009; Li and Wang, 2012; Yu et al., 2018). Inner rainbands are active in the inner core [roughly within the rapid filamentation zone (Rozoff et al., 2006)], characterized by relat-

ively smooth boundaries in reflectivity (Li and Wang, 2012). Those develop in the outer core (roughly outside the rapid filamentation zone) and are termed outer rainbands, ordinarily with embedded cellular convection exhibiting diverse degrees of organization (Barnes et al., 1983, 1991; Li and Wang, 2012).

Besides a variety of convective cells, there are visible stratiform clouds within TC outer rainbands. Two forms of stratiform clouds are generally observed in outer rainbands. One is the stratiform precipitation closely adjacent to dis-

* Corresponding author: Qingqing LI
Email: liqq@nuist.edu.cn

crete cellular convection (Barnes et al., 1983, 1991; Houze, 2010). This type of stratiform cloud is produced from weakening nimbostratus that forms due to the collapse of convective cells, as also illustrated in midlatitude and tropical thunderstorms (Yuter and Houze, 1995a,b). The other is the broad stratiform precipitation in the downwind sector of outer rainbands, occasionally with dying convective cells embedded (Atlas et al., 1963; Houze, 2010; Li and Wang, 2012; Didlake and Houze, 2013; Yu and Didlake, 2019). The latter regularly covers a broader area than the former. In the present study, we examine the characteristics of such stratiform clouds in the downwind sector of outer rainbands.

Previous studies have shown that the outer rainband stratiform sector may have spatial coverage that is even 10 times larger than the convective precipitation (Marks, 2003), and is characterized by a distinct bright band just below the 0°C isotherm due to the lower reflectivity of ice particles above the melting layer (Marks, 1985). Houze (1997) showed that net condensation heating dominates the whole troposphere in convective regions, while net condensation heating occurs only at upper levels in the stratiform region, and net cooling related to evaporation and melting arises in the lower troposphere. The downwind stratiform sector of outer rainbands exhibits weaker vertical velocity (May and Holland, 1999; Hense and Houze, 2008; Didlake and Houze, 2013), compared with convective cells. Accompanying the condensation heating features noted above, net downward (upward) mass transport is found below (above) midlevels in the stratiform sector (Didlake and Houze, 2013). Donaher et al. (2013) analyzed observations of landfalling TC stratiform rainbands and found that there is a horizontal wind speed peak between $z = 1$ and 1.5 km and a transition from TC-relative inflow to outflow near $z = 2.5$ –3 km.

Numerous studies have indicated that downwind stratiform clouds within outer rainbands play an important role in TC structure and intensity change. With diabatic cooling beneath the midtroposphere and diabatic heating high up in the stratiform clouds, positive potential vorticity anomalies are hence expected near midlevels. Several studies infer that a TC would intensify if the positive potential vorticity anomalies within outer rainband stratiform clouds are transported into the inner-core region (May and Holland, 1999; Franklin et al., 2006). Moon and Nolan (2010) demonstrated that the stratiform part of outer rainbands accounts for a strong secondary horizontal wind maximum and midlevel radial inflow that is moving down to the surface. As this descending inflow penetrates the inner core, the radial velocity gradient, and thus enhanced convergence, occur near the outer edge of the inner core, fostering local convection to even promote secondary eyewall formation (Qiu and Tan, 2013; Didlake et al., 2018). More recently, Yu and Didlake (2019) conducted idealized simulations to examine the response of wind fields to stratiform heating profiles of a typical stationary principal rainband, and also found the presence of descending inflow and a tangential jet.

As an important environmental factor affecting TC struc-

ture and intensity change, large environmental vertical wind shear (VWS) is documented to be generally detrimental to TC intensification (DeMaria, 1996; Wong and Chan, 2004; Paterson et al., 2005; Hendricks et al., 2010; Riemer et al., 2010; Zeng et al., 2010; Wang et al., 2015) and suppresses the TC maximum intensity (Braun and Wu, 2007; Tang and Emanuel, 2010, 2012). Additionally, VWS can force a variety of structural asymmetries within the TC circulation, including, but not limited to, azimuthally asymmetric convection in the inner core (Marks et al., 1992; Franklin et al., 1993; DeMaria, 1996; Frank and Ritchie, 1999, 2001; Corbosiero and Molinari, 2003; Reasor, 2004; Heymsfield et al., 2006; Li et al., 2008; Xu and Wang, 2013), shear-relative asymmetries in eyewall slope (Hazelton et al., 2015), asymmetric wind distribution (Uhlhorn et al., 2014; Gu et al., 2016), and wavenumber-1 outer rainbands (Li et al., 2017).

Recently, an increasing number of studies have also focused on the responses of TC structure and intensity to the vertical profile of VWS (Paterson et al., 2005; Zeng et al., 2010; Shu et al., 2013; Reasor et al., 2013; Onderlinde and Nolan, 2014; Velden and Sears, 2014; Wang et al., 2015; Finocchio and Majumdar, 2017; Rio-Berrios and Torn, 2017; Fu et al., 2019). Shu et al. (2013) documented that the intensity change of western North Pacific typhoons is more dependent on VWS between 850 hPa and 10-m height. Wang et al. (2015) further compared the relationships between TC intensity change and VWS in the western North Pacific and the North Atlantic, and they found a more significant negative correlation between the intensity change and 850–1000-hPa VWS in the western North Pacific, in contrast to a more significant negative correlation between the intensity change and deep-layer VWS in the North Atlantic. The numerical results in Finocchio et al. (2016) showed that low-level VWS is less favorable for the intensification of the TC. They documented that low-level shear tilts the vortex more effectively and facilitates a radially inward intrusion of low equivalent potential temperature (θ_e) air from the midlevel environment, thus frustrating the realignment and intensification of the TC. Furthermore, Finocchio and Majumdar (2017) found that upper-level shear is slightly more favorable for TC intensification by analyzing reanalysis data. However, Fu et al. (2019) suggested that, based on idealized numerical experiments, a TC in upper-layer shear tends to weaken more rapidly compared with a storm in lower-layer shear, because of the greater ventilation of the warm upper-level core by higher shear-forced asymmetric outflow in the upper-layer shear experiment. The different responses of TC intensity change to shear height between Finocchio et al. (2016) and Fu et al. (2019) are possibly because of the different environmental flow vertical profiles utilized in the numerical experiments and storm-relative flow in the inner core in the two studies.

Li et al. (2017) documented that VWS tends to produce wavenumber-1 quasi-stationary outer rainbands in the downshear quadrant, and the downwind stratiform sector of the outer rainbands is therefore persistently located left-of-

shear. The structural characteristics of the stratiform rainband in VWS deserve further elaboration since there exist significant vortex-scale kinematic responses to stratiform clouds within outer rainbands (Moon and Nolan, 2010; Yu and Didlake, 2019). In particular, whether there are distinct differences in the structure of the stratiform sector of outer rainbands in lower-layer and upper-layer VWS is open to question. We put forward a hypothesis that larger shear-forced asymmetric outflow in upper layers in the upper-layer shear experiment enables more advection of water vapor in upper layers in the downshear outer core, more conducive to the formation of ice-phase clouds and thus a better-organized stratiform sector in outer rainbands. This study aims to investigate the specific features of downwind stratiform rainband structures in TCs embedded in lower-layer and upper-layer VWS environments and examine the hypothesis raised above by using idealized numerical simulations. In section 2, we describe the model and experimental design. The classification of the stratiform sector of outer rainbands is introduced in section 3. In section 4, we discuss the structural characteristics of the stratiform sector. The conclusions are given in section 5.

2. Model and experimental design

The numerical experiments here are conducted using the fully compressible, nonhydrostatic model TCM4 (Wang 2007). Three model domains are quadruply nested with two-way interactive nesting. The domains have 241×201 , 127×127 , 163×163 , and 313×313 grid points, with horizontal grid spacings of 54, 18, 6, and 2 km, respectively, and the vertical grid has 32 levels. The model is conducted on an f plane at 18°N over the ocean with fixed sea surface temperatures of 29°C . The initial symmetric vortex has a maximum tangential wind speed of 18 m s^{-1} at the 90-km radius near the surface and decreases with pressure to vanish at 100 hPa in a sinusoidal manner. Given that the convection occurs mainly within the radius of 300 km from the storm center, no cumulus parameterization is used. The initial thermodynamic profile of the unperturbed model atmosphere is derived from the moist-tropical sounding of Dunion (2011). Those interested in the model and the modeling framework can see the details in Wang (2007) and Li and Fang (2018).

After the initial weak TC is spun up for 60 h, easterly VWS of 10 m s^{-1} is introduced into the simulation. At this time, the simulated minimum sea level pressure of the TC is about 965 hPa with a radius of maximum surface wind of approximately 35 km (Fig. 1). For convenience, this time is designated as 0 h hereafter. The vertical profiles of the VWS are shown in the inset in Fig. 1. In the first experiment (hereafter LOSH), the environmental zonal wind increases from 0 m s^{-1} at approximately $z = 1.5 \text{ km}$ to 10 m s^{-1} above approximately $z = 5 \text{ km}$, indicating a lower-layer moderate shear environment. In the second experiment (hereafter UPSH), the environmental zonal wind starts increasing from 0 m s^{-1} at approximately $z = 7.3 \text{ km}$ to 10 m s^{-1} above approximately $z = 13.5 \text{ km}$, suggestive of an upper-

layer moderate shear environment. Note that the background flow is nearly windless in the boundary layer in the two shear profiles (Fig. 1), which is purposefully designed to refrain from any possible interaction of the background flow with the boundary layer. The environmental flow is in geostrophic and hydrostatic balance and is maintained through the lateral boundary conditions during the integration. LOSH and UPSH are then integrated for 48 h. The environmental VWS is nearly maintained throughout the 48-h simulation (not shown).

Figure 1 shows that the storm modeled in LOSH tends to intensify slowly with intensity oscillations. Such intensity pulses are likely due to the boundary-layer entropy decrease and recovery associated with the activity of outer spiral rainbands (Fu et al., 2019). The minimum sea level pressure of the storm in LOSH finally drops to 935 hPa. The storm in UPSH intensifies not as rapidly as in LOSH after the VWS is introduced. The minimum sea level pressure of the TC in UPSH drops to 948 hPa at 48 h. The reduction of TC intensification rate in the upper-layer shear experiment is caused by the significant ventilation of the warm core at upper levels, as recently documented in Fu et al., (2019).

3. Identification and classification of the stratiform sector

For the sake of examining the features of the outer rainband stratiform sector, a convective–stratiform partitioning method is needed. In this paper, the algorithm used in Rogers (2010) is applied to conduct the convective–stratiform partitioning. This algorithm depends mainly on the horizontal distribution of radar reflectivity together with low-level updraft characteristics and has shown good feasibility with respect to convective–stratiform partitioning for high-resolution numerical simulation results (Rogers, 2010; Li and

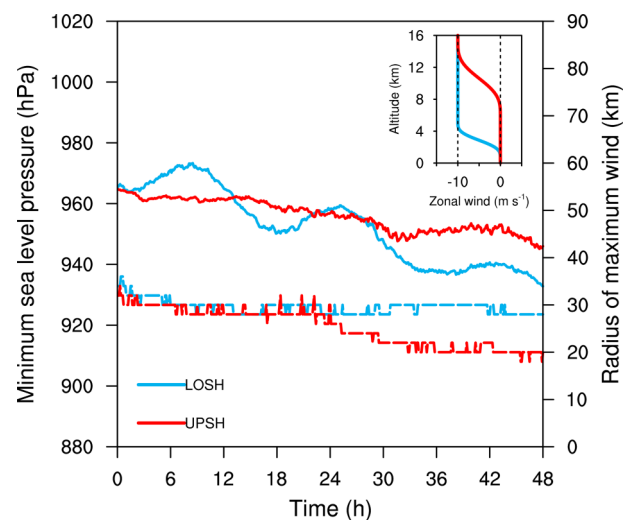


Fig. 1. Time series of the simulated minimum sea level pressure (solid lines) and RMW (dashed lines). The inset shows the vertical profiles of environmental zonal winds employed in LOSH and UPSH.

Wang, 2012; Chen et al., 2018). This convective–stratiform partitioning algorithm can categorize precipitation grids as convective, stratiform, and other (anvil-type) precipitation. The algorithm is described at length in Rogers (2010).

Figure 2 shows the 3-km-height radar reflectivity in LOSH at 6 h (Fig. 2a) and in UPSH at 37 h (Fig. 2b), along with the corresponding convective–stratiform partitioning results (Figs. 2c and d). The modeled principal rainbands are located downshear, and stronger inner-core convection tends to occur left-of-shear (Figs. 2a and b), consistent with the results of previous studies. Figures 2c and d clearly show that numerous isolated convective cells populate the upwind and middle portions of the outer rainbands, whereas broad strati-

form precipitation with sporadic cellular convection embedded occupies the downwind sector, specifically on the left of VWS. These outer rainband cloud traits agree with the results of prior studies (Houze, 2010; Li and Wang, 2012), with nascent convective cells in the upwind portion of outer rainbands, mature cells in the middle part, and stratiform clouds along with collapsing cells in the downwind sector.

A further investigation of the snapshots of reflectivity indicates that much stronger cellular convection tends to occur in the outer rainbands in LOSH, compared to UPSH (not shown). Similar characteristics of outer rainband convective activity were also found in Fu et al. (2019). The presence of more intense convective cells in the outer rainbands

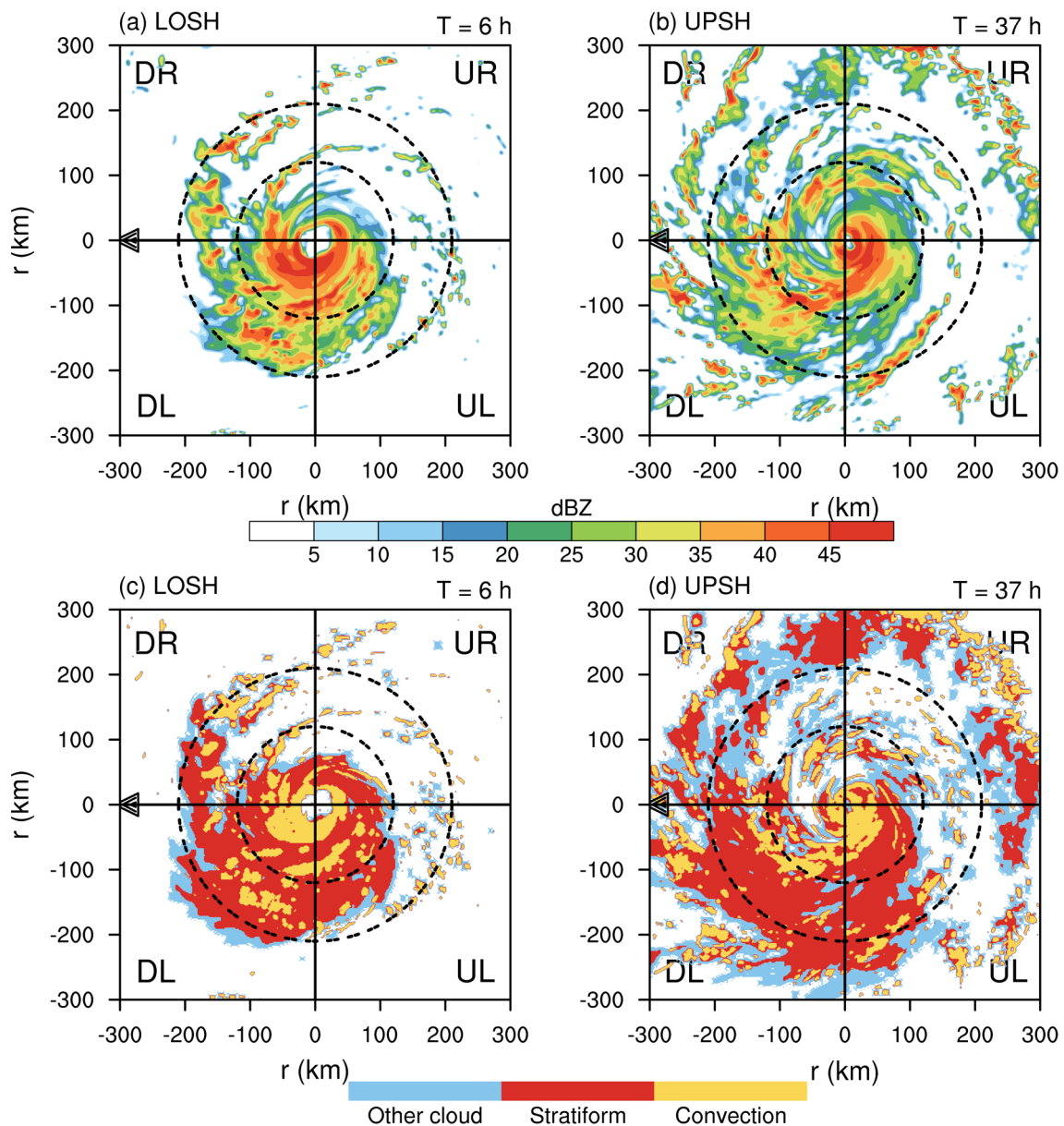


Fig. 2. Simulated radar reflectivity at $z = 3$ km for (a) LOSH at 6 h and (b) UPSH at 37 h. The convective–stratiform partitioning results at the same times are shown in (c) and (d), respectively. The inner and outer black dashed circles denote four and seven times the RMW, respectively. The black arrow indicates the easterly VWS. “UL”, “UR”, “DR”, and “DL” indicate the upshear-left, upshear-right, downshear-right, and downshear-left quadrants, respectively.

in LOSH likely results from the dynamical interaction between near-surface cold pools and lower-level wind shear, according to the cold pool dynamics (Rotunno et al., 1988). As the horizontal vorticity generated by the lower-layer shear effectively counteracts the horizontal vorticity generated by the cold pool, intense and vertically upright convection arises in the front of the cold pool. Because evident shear exists at low levels in LOSH, the convective intensity of the outer rainbands is likely strong in this experiment. The corresponding details are not examined here, given that the subject of the current study is to investigate the dynamic and thermodynamic differences in stratiform rainbands. The mechanisms for the different convective activity in the outer rainbands in the two experiments will be discussed in a follow-up study.

The characteristics of stratiform clouds in the downwind sector of the outer rainbands are the focus of this study, so we need to appropriately identify the downwind stratiform rainbands. Outer rainbands are regularly active outside the inner core, which is no more than 3–4 times the radius of maximum wind (RMW; Wang, 2009; Li and Wang, 2012; Li et al., 2017). Therefore, those spiral rainbands that are more than four times the RMW are taken as the outer rainbands in the current study. Figure 1 suggests that the RMW in LOSH and UPSH ranges mainly between 20 and 30 km, and the outer rainbands simulated in the two experiments are hence located beyond approximately 80 km from the storm center. Figure 3 indeed shows that signals of axisymmetric surface rain rates initiate near the radius of 80 km and slowly propagate radially outward, indicative of the activity of outer rainbands. A radius of seven times the RMW is chosen as the outer boundary of the downwind stratiform sector of the outer rainbands of interest. Figures 2c and d demonstrate that the outer rainband stratiform sectors are mostly bounded by four and seven times the RMW in the downshear-left and upshear-left quadrants.

To further identify the range of the downwind strati-

form sector, the following procedures are carried out: If stratiform grids occupy at least half a 30° sectorial region between four and seven times the RMW, this region is first chosen as a candidate of the stratiform sector. This criterion means that stratiform clouds must cover more than half of the sectorial area. Given that the stratiform portion steadily lies in the downwind part of the quasi-stationary principal rainband (Hence and Houze, 2008; Houze, 2010; Didlake and Houze, 2013), those stratiform candidates that show spatial continuity in the azimuthal direction and exist for at least three hours are treated as the stratiform sector of the principal rainband. Additionally, observations indicate that there are anvil-type clouds and dying convective cells occasionally embedded in the stratiform portion, as also shown in Figs. 2c and d. Therefore, three stratiform sector groupings are defined. If more than 75% of the all grids in the stratiform sector manifest as stratiform clouds, such a sector is termed the stratiform-dominant (SD) part. If stratiform grids are less than 75% of the all grids and convective grids are more than anvil-type grids, this stratiform sector is designated as the convection-concomitant stratiform (CCS) part. The third type refers to the stratiform sector, within which stratiform grids are less than 75% of the all grids and convective grids are less than anvil-type grids. This stratiform sector type is termed the anvil-concomitant stratiform (ACS) part. For concise expressions, the aforementioned stratiform types in the two experiments are abbreviated in the following context. For example, the SD part in LOSH is abbreviated to SD-LOSH, and so forth.

Figure 4 shows the time–azimuthal distribution of the identified stratiform rainbands in the two experiments. The stratiform sector of the outer rainbands is located mostly downshear left, subtly shifting downwind to the upshear-left quadrant in UPSH after 36 h. Note that the stratiform sector in LOSH can be identified successfully only between 3 and 10 h (Fig. 4a) based on the criteria mentioned above. This is because the outer rainbands in LOSH seem to be less active

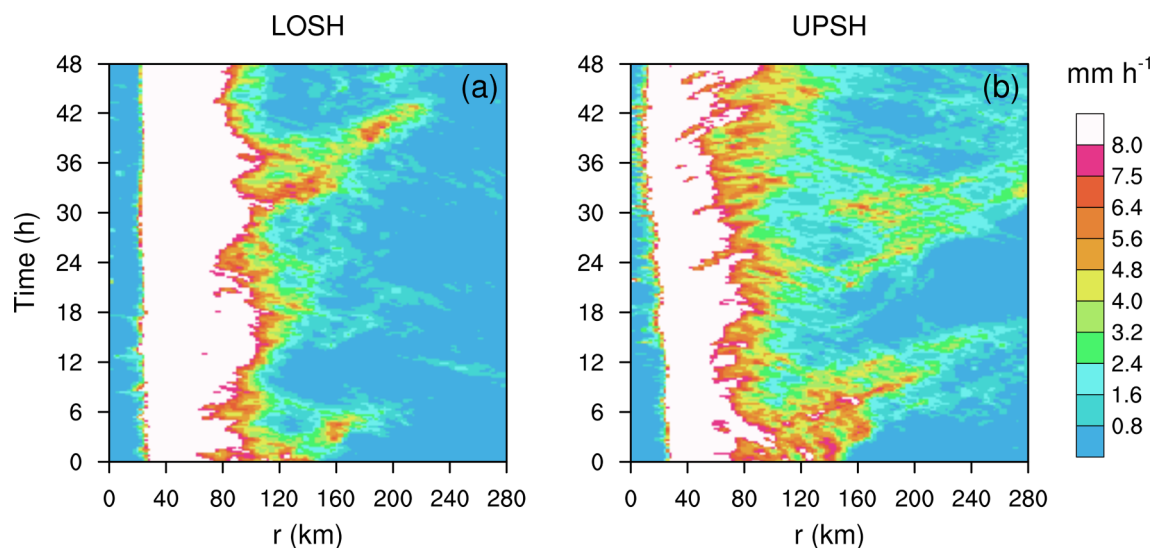


Fig. 3. Radius–time Hovmöller diagram of the rainfall rate in (a) LOSH and (b) UPSH. Note that values of greater than 8 mm h^{-1} are whited out.

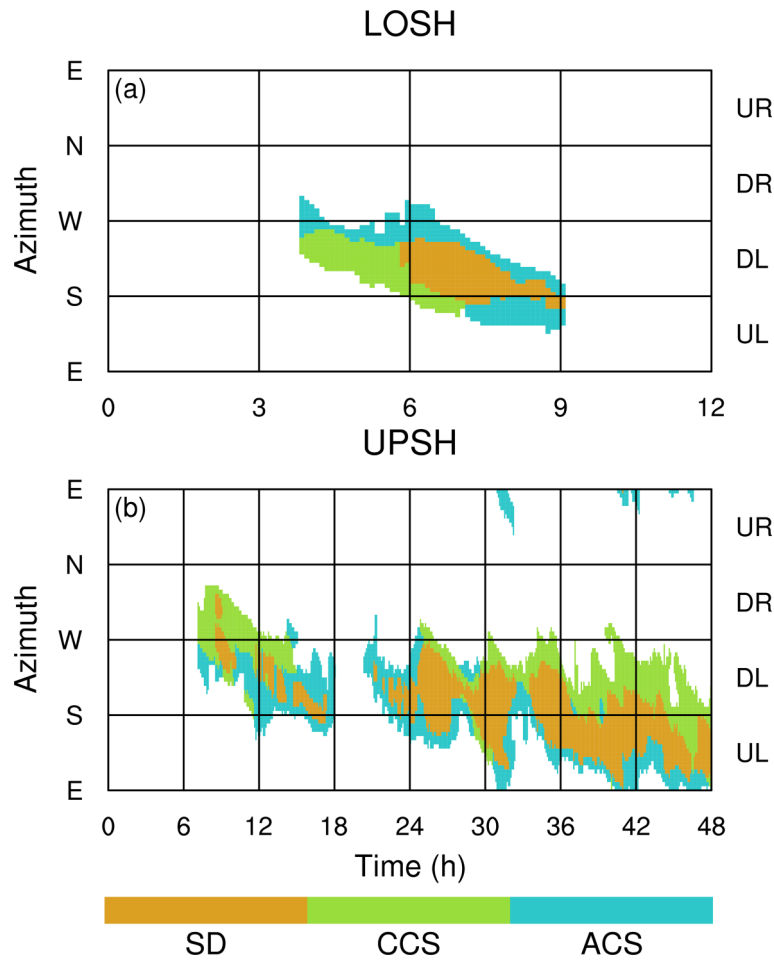


Fig. 4. Time–azimuthal Hovmöller diagram of the identified outer rainband stratiform sector in (a) LOSH and (b) UPSH. “SD”, “CCS”, and “ACS” denote the stratiform-dominant, convection-concomitant, and anvil-concomitant parts, respectively, as detailed in the text (section 3).

than those in UPSH (Fig. 3) and the stratiform precipitation in the outer rainbands in LOSH is less organized. The stratiform sector of the outer rainbands in UPSH shares patterns with typical stratiform rainbands in previous studies (Hence and Houze, 2008; Houze, 2010; Didlake and Houze, 2013), generally with limited CCS upwind, broad SD in the middle, and small ACS downwind (Fig. 4b). This cloud pattern likely illustrates that as convective cells are cyclonically moving in the downwind sector of the outer rainband, they tend to decay into stratiform clouds that subsequently weaken into anvil clouds. By contrast, the clouds of the outer rainband stratiform sector in LOSH do not exhibit a typical CCS-SD-ACS feature (Fig. 4a), possibly because the outer rainbands modeled in that experiment are less active as mentioned above.

4. Characteristics of the downwind stratiform sector

4.1. Precipitation features

Figure 5 shows the contoured frequency by altitude dia-

grams (CFADs; Yuter and Houze, 1995) of reflectivity of the stratiform sector, which display the frequency distribution of reflectivity [per bin size (~ 0.5 km \times 5 dBZ)] as a function of height. The reflectivity traits of the stratiform sector in the two experiments are similar below $z = 5$ km, with most reflectivity values centered on about 31 dBZ in SD (Figs. 5a and d), 34 dBZ in CCS (Figs. 5b and e), and 28 dBZ (Figs. 5c and f) in ACS. The highest reflectivity is observed in CCS, with values exceeding 50 dBZ (Figs. 5b and e). Figure 6 indicates rainwater contributing mainly to the precipitation below the midtroposphere. Medium, high, and weak rainwater is present in SD (Figs. 6a and d), CCS (Figs. 6b and e), and ACS (Figs. 6c and f), respectively. A bright band is notable near $z = 5$ km, coincident with findings of previous studies (Marks, 1985; Didlake and Houze, 2013). Between $z = 5.5$ and 11 km, most reflectivity in the stratiform sector ranges between 20 and 30 dBZ (Fig. 5). Figure 6 indicates that a great deal of graupel along with ice and snow corresponds to the maximum CFADs at these heights, and medium, high, and weak graupel occurs in SD (Figs. 6a and d), CCS (Figs. 6b and e), and ACS (Figs. 6c and f), respectively. The significant distinction of reflectiv-

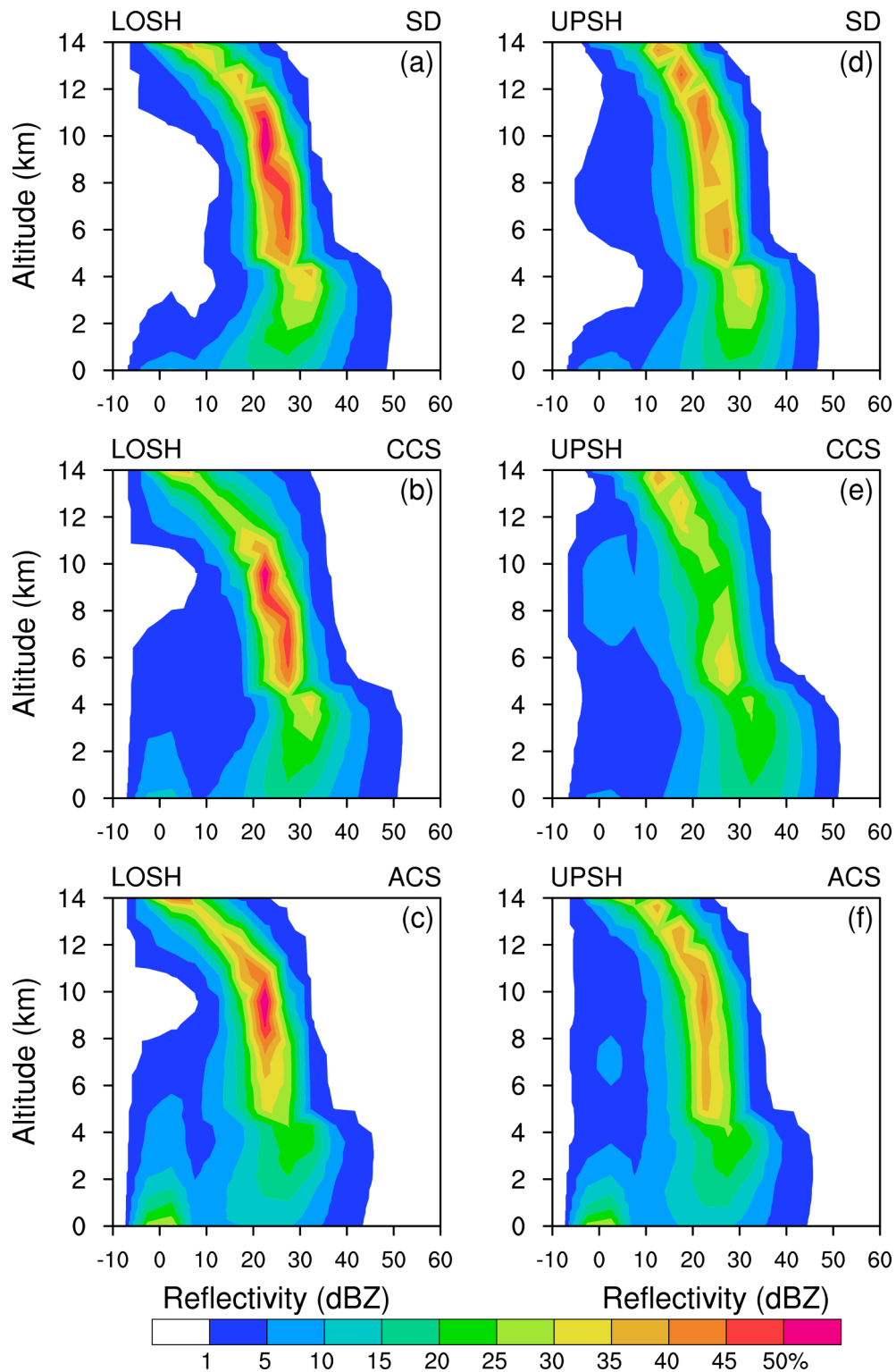


Fig. 5. CFADs of radar reflectivity (in bins of 5 dBZ) for (a–c) LOSH and (d–f) UPSH, in (a, d) SD, (b, e) CCS, and (c, f) ACS.

ity CFADs in the outer rainband stratiform sector between LOSH and UPSH at heights of 5.5–11 km is the presence of reflectivity of < 20 dBZ in SD-, CCS-, and ACS-UPSH versus the absence of such reflectivity values in SD-, CCS-, and ACS-LOSH (Fig. 5). The increased amount of relatively weak radar reflectivity in the stratiform sector in

UPSH is subject to more graupel as well as cloud ice at upper levels (e.g., above $z = 9$ km; Figs. 6d–f), compared with LOSH (Figs. 6a–c). Figure 7 depicts the horizontal distributions of the mixing ratio of water vapor and asymmetric flow vertically averaged between $z = 8.6$ and 10.6 km and temporally averaged between 3 and 10 h for LOSH (Fig. 7a),

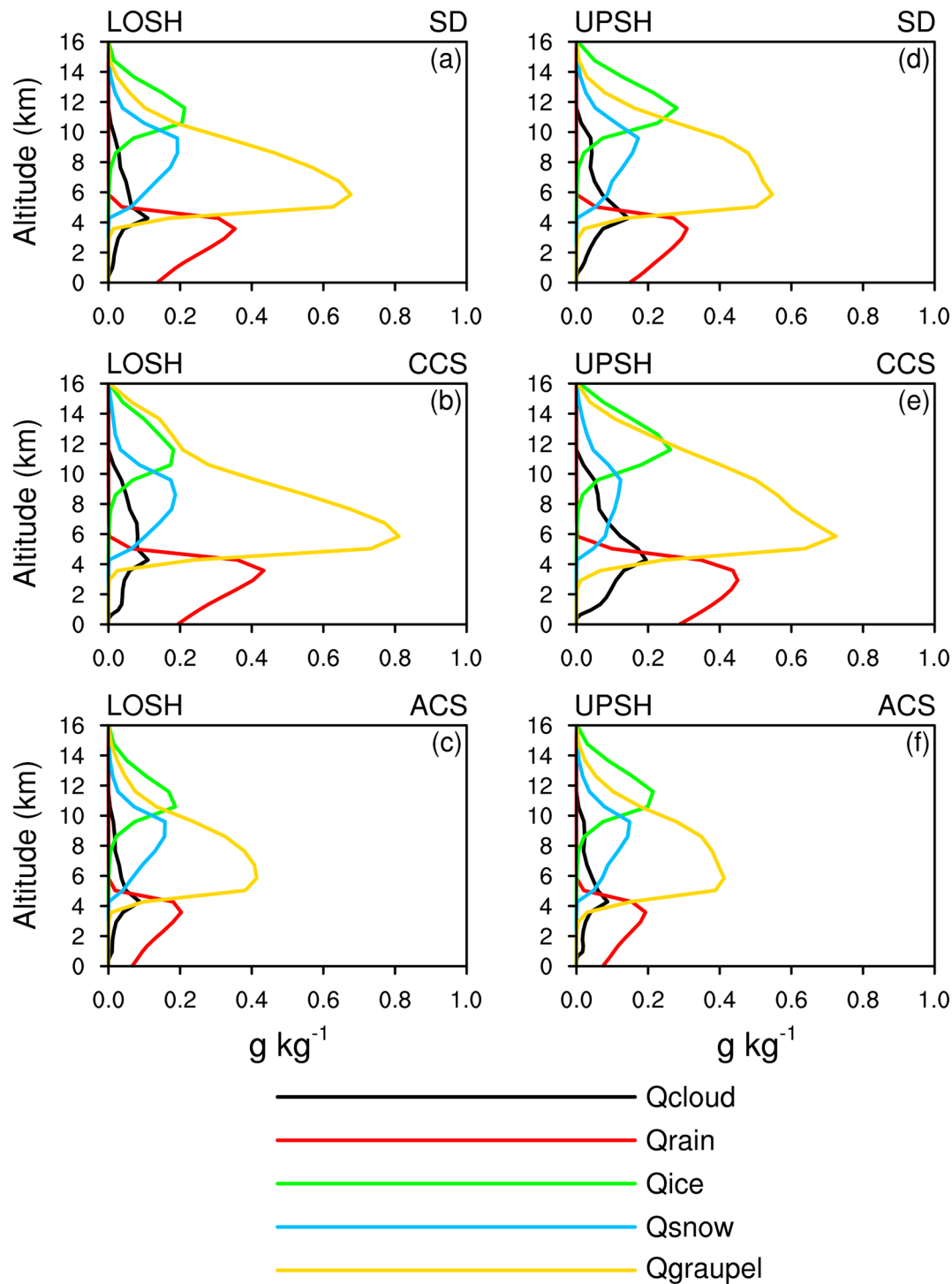


Fig. 6. Vertical profiles of the mixing ratios of cloud (black), rainwater (red), cloud ice (green), snow (blue), and graupel (yellow) averaged in (a, d) SD, (b, e) CCS, and (c, f) ACS, for (a–c) LOSH and (d–f) UPSH.

and between 6 and 48 h for UPSH (Fig. 7b). The storm-relative asymmetric flow is defined as the relative flow across the cyclone circulation (Willoughby et al. 1984; Bender 1997; Frank and Ritchie 2001), including not only the environmental flow but also the asymmetric flow owing to the interaction between the TC and VWS. The storm-relative asymmetric flow is governed initially by the difference between the environmental wind and TC motion. Given that

the environmental steering levels usually lie at midlevels, the steering flow is much weaker in UPSH than in LOSH (Fig. 1). Therefore, the storm in UPSH moves much more slowly than that in LOSH (not shown), and the upper-level asymmetric outflow in the downshear-left quadrant is stronger in UPSH (Fig. 7b) than in LOSH (Fig. 7a), coincident with the results in Fu et al. (2019). Such stronger asymmetric outflow radially outward advects more moisture

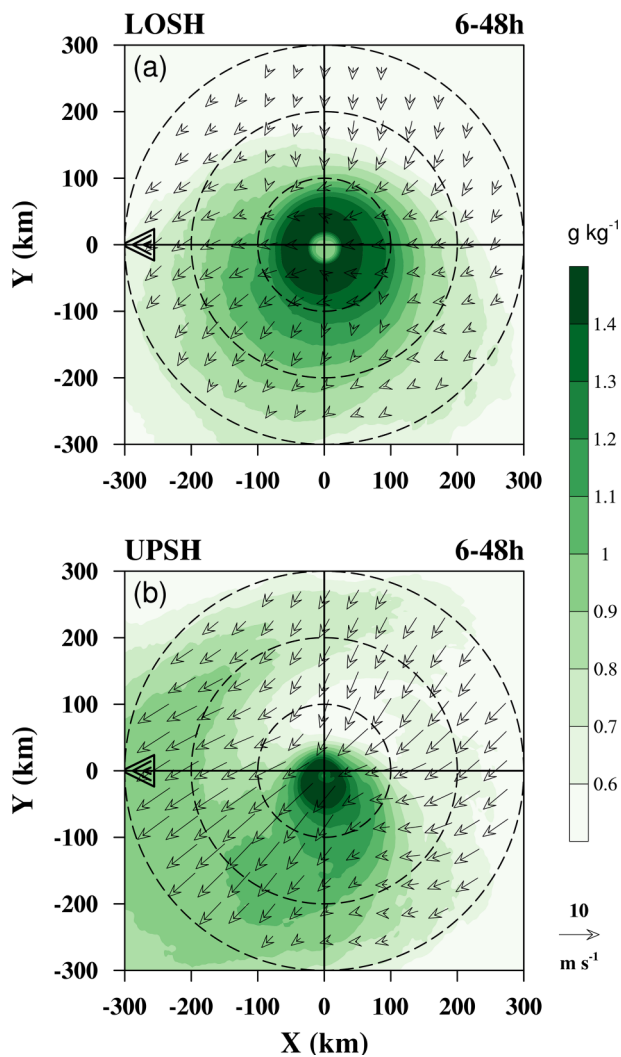


Fig. 7. The mixing ratio of water vapor (shading) and asymmetric winds (vectors) vertically averaged between $z = 8.6$ and $z = 10.6$ km in (a) LOSH and (b) UPSH, temporally averaged from 6 to 48 h.

from the inner core to the outer core in the downshear-left outer core in UPSH (Fig. 7b). Resultingly, the upper-level air in the downshear-left outer core in UPSH (Fig. 7b) is more humid than in LOSH (Fig. 7a). More depositional growth of both graupel and cloud ice (Wang, 2001) thus occurs, accounting for more graupel and cloud ice at upper levels in the stratiform sector of the outer rainbands in UPSH (Figs. 6d–f). Moreover, the outer rainband stratiform clouds in UPSH are hence better-organized than those in LOSH. The above results corroborate the hypothesis in the introduction that stronger asymmetric outflow forced by upper-layer VWS may largely influence the structure of the outer rainband stratiform sector.

4.2. Kinematic traits

Figure 8 shows the CFADs of vertical velocity in the stratiform sector. In SD, a downward velocity of approximately -0.2 m s^{-1} is dominant below $z = 5$ km in both the experiments (Figs. 8a and d). However, the mean downdraft mass

transport normalized by the maximum mean updraft mass transport, particularly near $z = 2\text{--}3$ km, is larger in SD-UPSH (Fig. 9d) than that in SD-LOSH (Fig. 9a). As a result, significant subsidence indicated by downward net vertical mass transport exists below $z = 3$ km in SD-UPSH (Fig. 9d), as found in Didlake and Houze (2013), while much weaker negative net vertical mass transport occurs below $z = 0.5$ km in SD-LOSH (Fig. 9a). The above result implies deeper and stronger descending motions in the lower layers of SD-UPSH. Although marked upward net vertical mass transport occurs in SD between $z = 6$ and 12 km in both the experiments (Figs. 9a and d), more and stronger upward motions appear above $z = 8$ km in SD-UPSH (Fig. 8d). Such stronger updraft motions in the upper layers of SD are associated with greater diabatic heating from the deposition of graupel in UPSH.

The distribution of vertical velocity CFADs in CCS resembles that in SD-LOSH (Fig. 8b), just with stronger upward motions (e.g., vertical velocity $> 1 \text{ m s}^{-1}$) in CCS. More upward motions with weak vertical velocity (e.g., vertical velocity $< 0.4 \text{ m s}^{-1}$) are found in CCS-UPSH (Fig. 8e), compared with those in CCS-LOSH (Fig. 8b). Upward net mass transport thereby exists throughout the troposphere in both CCS-LOSH and CCS-UPSH (Figs. 9b and e), indicative of the presence of convective cells that are generally dying convection embedded in the stratiform clouds. Note that the upward velocity and positive mass transport between $z = 8$ and 10 km in CCS-UPSH (Figs. 8e and 9e) are also higher than those in CCS-LOSH (Figs. 8b and b), again demonstrative of greater diabatic heating from the deposition of graupel in CCS-UPSH. In ACS, the features of vertical velocity CFADs and normalized vertical mass transport (Figs. 8c, f, 9c, and f) are analogous to those in SD.

Figure 10 shows the vertical distribution of averaged divergence in SD, CCS, and ACS, along with the upper and lower quartiles of divergence magnitude. The interquartile range of the divergence of the outer rainband stratiform sectors is large, and the mean divergence shows several differences among SD, CCS, and ACS, particularly within the boundary layer. Because the SD downward motion at lower levels in UPSH is deeper and stronger than that in LOSH (Figs. 9a and d), the divergence layer immediately above the surface in SD-UPSH is deeper (approximately below $z = 1.8$ km; Fig. 10d) than that in SD-LOSH (approximately below $z = 1.5$ km; Fig. 10a). Above that divergence layer, the vertical distributions of mean divergence are similar in the two experiments, with convergence between $z = 2$ and 9 km and divergence between $z = 9$ and 15 km (Figs. 10a and d). The sandwiched convergence results from the confluence of inflow radially outside the rainband and outflow inside the band (discussed later), which is associated with the enhanced latent heating in the middle and upper layers.

Such a divergence–convergence–divergence structure of mean divergence is not visible in CCS (Figs. 10b and e), particularly without divergence in the boundary layer in CCS-UPSH (Fig. 10e), consistent with the absence of down-

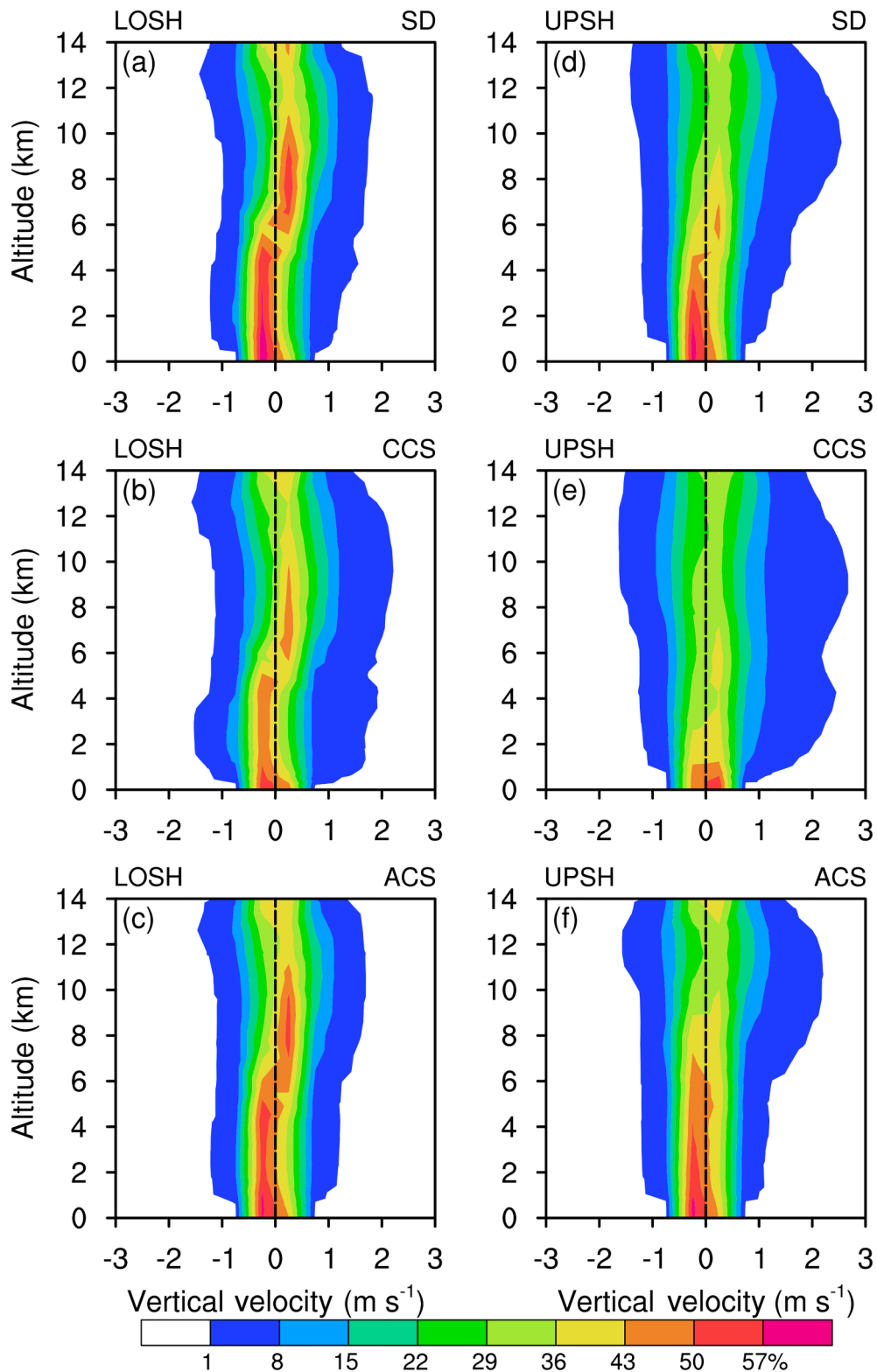


Fig. 8. CFADs of vertical velocity (in bins of 0.5 m s⁻¹) for (a–c) LOSH and (d–f) UPSH, in (a, d) SD, (b, e) CCS, and (c, f) ACS.

ward net mass transport in the boundary layer (Figs. 9b and e). In ACS, the sandwich structure of divergence is present, with a deeper convergence layer and a shallower divergence layer high up (Figs. 10c and f).

Figure 11 displays the vertical distribution of averaged

radial velocity in the stratiform sectors, showing relatively limited interquartile ranges. In LOSH, there is inflow approximately below $z = 3.5$ km, outflow between $z = 4$ and 15.5 km, and inflow high up (Figs. 11a–c). In UPSH, the lower-level inflow layer (Figs. 11d–f) is deeper than that in

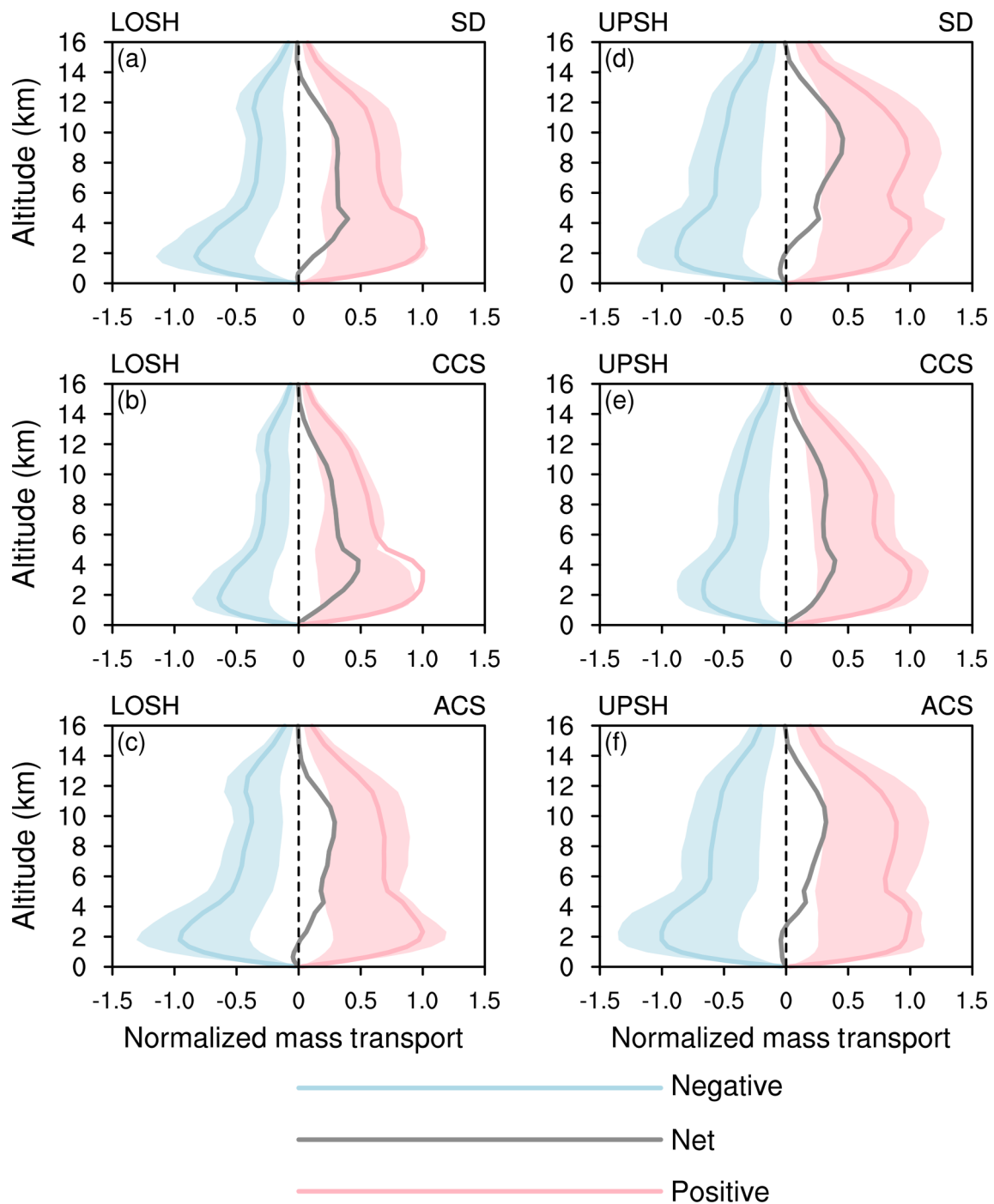


Fig. 9. Vertical profiles of mean upward (blue line), downward (red line), and net (grey line) vertical mass transport for (a–c) LOSH and (d–f) UPSH, along with the upper and lower quartiles of upward (light blue shading) and downward (light red shading) vertical mass transport, in (a, d) SD, (b, e) CCS, and (c, f) ACS. The average values are normalized by the maximum upward mass transport.

LOSH. For instance, the inflow layer in ACS-UPSH can extend from the surface to $z = 7.7$ km (Fig. 11f). The above radial velocity patterns, along with the vertical mass transport characteristics (Fig. 9), reveals that descending inflow occurs below the midlevels in the stratiform sector of outer rainbands (Moon and Nolan, 2010; Qiu and Tan, 2013; Didlake et al., 2018; Yu and Didlake, 2019). The radial velocity structure resembles the observations in Donaher et al.

(2013). In particular, the descending inflow layer is deeper in UPSH than that in LOSH, with the peak inflow around 300 m above the surface.

The idealized simulations in Moon and Nolan (2010) and Yu and Didlake (2019) documented that there are significant radial flow responses to stratiform-type diabatic heating. The diabatic heating distribution, similar to observations, tends to produce strong midlevel outflow on the radially

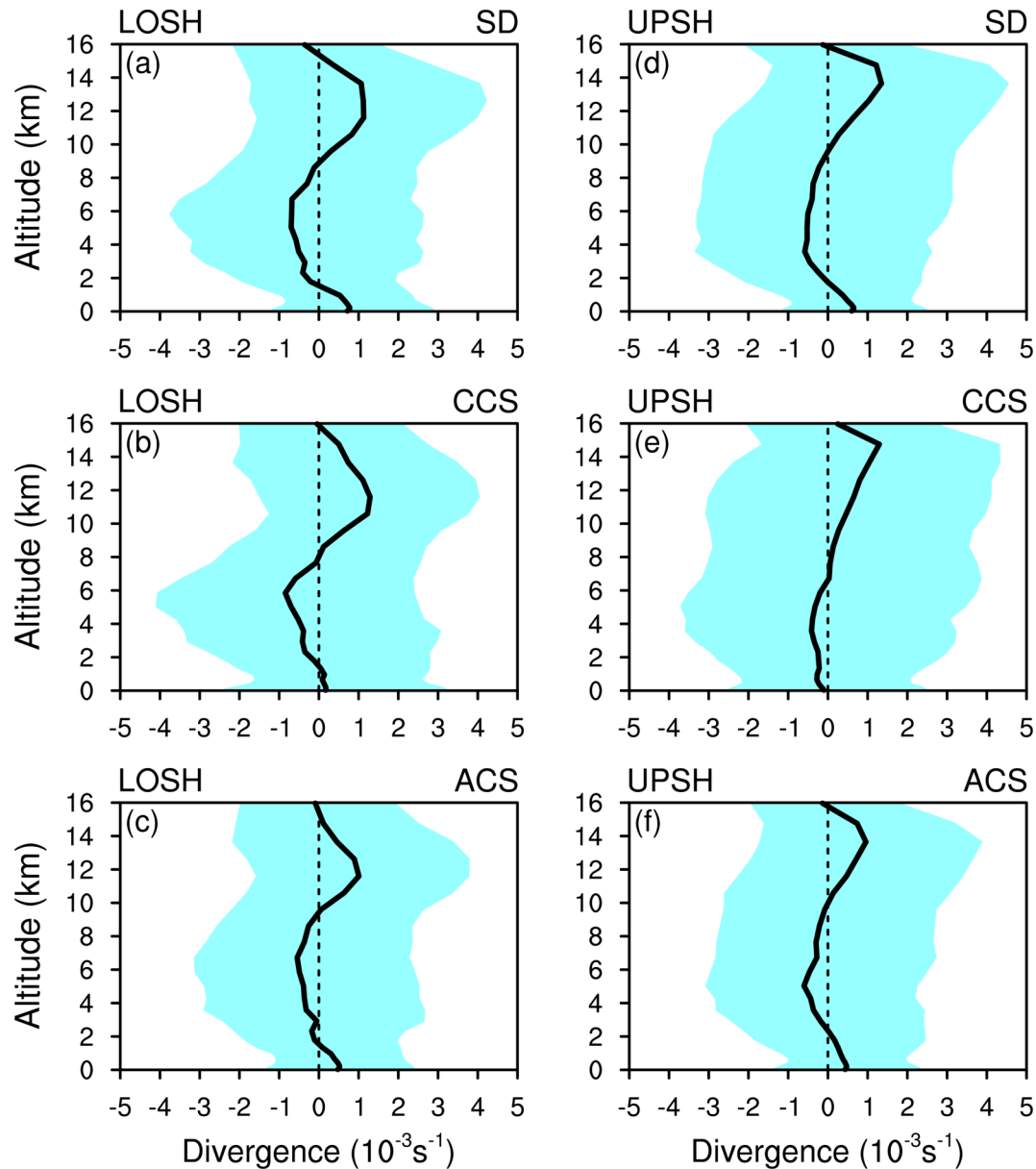


Fig. 10. Vertical profiles of averaged divergence (black line) for (a–c) LOSH and (d–f) UPSH, along with the upper and lower quartiles (light blue shading), in (a, d) SD, (b, e) CCS, and (c, f) ACS.

inward side of the heating core in stratiform clouds and weak midlevel inflow on the radially outward side of the heating core, with lower-level inflow beneath the midlevel outflow and upper-level inflow above (Yu and Didlake, 2019). It is difficult to quantitatively evaluate the stratiform diabatic heating–induced radial velocity based on the current simulations. Alternatively, the asymmetric radial velocity can be utilized to examine the possible role of diabatic heating in the stratiform sector in modulating the local radial motions, although the asymmetric radial velocity also encompasses the response to the downshear interaction between the VWS and the vortex circulation. Figure 12 shows the asymmetric radial velocity averaged in SD, CCS, and ACS in the two experiments. Asymmetric inflow, outflow, and inflow occur below $z = 3.5$ km, between $z = 3.5$ and 11 km, and above $z = 11$ km in the stratiform sector of the TC outer

rainbands in LOSH, respectively (Figs. 12a–c). Because the VWS should force asymmetric outflow in the downshear-left upper layers (Figs. 7a; Braun et al., 2006; Wu et al., 2006), the signal of asymmetric inflow above $z = 11$ km in the stratiform sector in LOSH (Figs. 12a–c) presents the likelihood of stratiform diabatic heating–forced inflow being predominant in the upper layers during 3–9 h, as demonstrated in Fig. 11 in Yu and Didlake (2019). Correspondingly, the lower-level inflow and midlevel net outflow associated with the stratiform diabatic heating (Yu and Didlake, 2019), together with the shear-forced lower-level inflow and outflow above in the downshear-left quadrant, may contribute to the asymmetric inflow below $z = 3.5$ km and the asymmetric outflow between $z = 3.5$ and 11 km in LOSH (Figs. 12a–c). By contrast, the lower-level asymmetric inflow layer in the stratiform sector is deeper in UPSH (Figs. 12d–f) than in

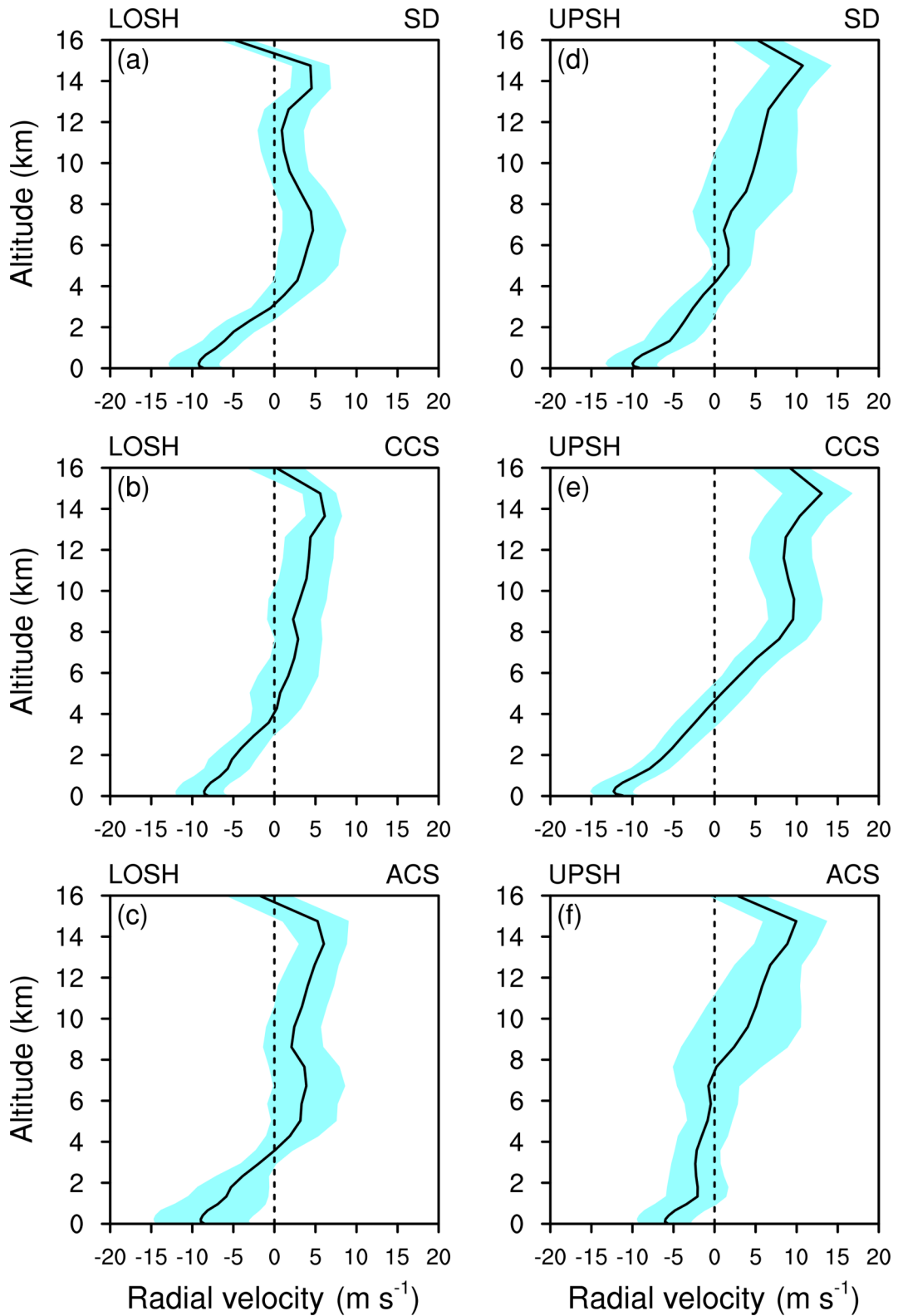


Fig. 11. As in Fig. 10, but for radial velocity.

LOSH, indicating that upper-layer VWS tends to produce a deeper asymmetric inflow layer in the downshear quadrant. Above the asymmetric inflow is the asymmetric outflow in UPSH, with enhanced asymmetric outflow around $z = 5\text{--}9$ km and reduced asymmetric outflow near $z = 9\text{--}15$ km, par-

ticularly in SD and CCS (Figs. 12d and e). This asymmetric outflow structure likely reflects the role of stratiform diabatic heating-induced upper-level outflow and midlevel inflow on the radially inward side of the heating core (Yu and Didlake, 2019). A comparison of the asymmetric radial

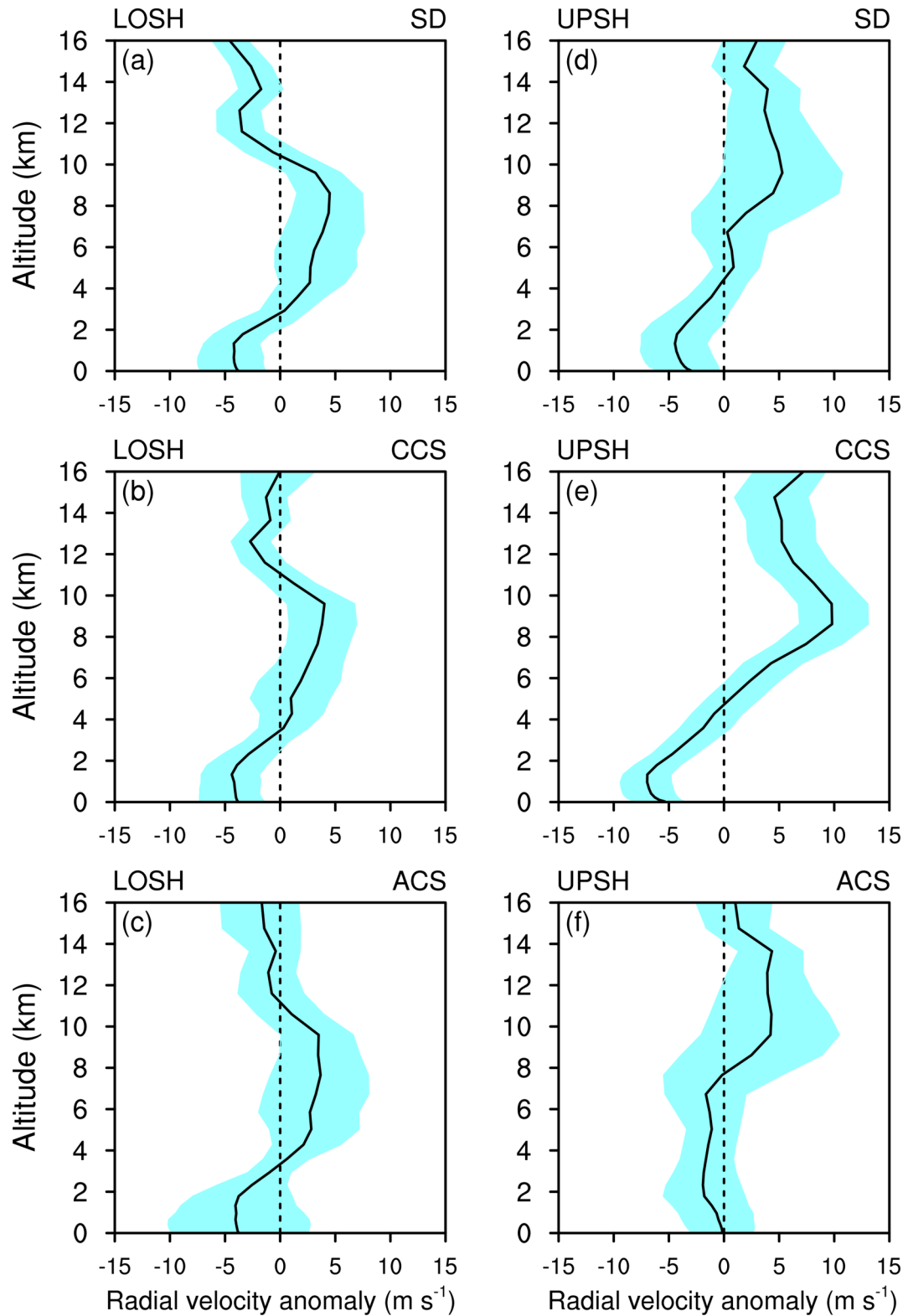


Fig. 12. As in Fig. 10, but for asymmetric radial velocity.

velocity averaged within the stratiform sector also shows that the lower-level asymmetric inflow jet structure is more pronounced in UPSH than in LOSH (near $z = 1\text{--}1.5$ km; Fig. 12), particularly in SD and CCS, seemingly suggesting more significant stratiform-induced descending inflow in UPSH. Note that the heights of the signals of stratiform-

forced midlevel outflow and upper-level inflow both in LOSH and UPSH are much higher than the results in Yu and Didlake (2019), possibly resulting from the stratiform heating that lies at a higher altitude in the present simulations and will be discussed later.

Many observational and numerical simulation studies

have documented that there is generally a tangential jet in the stratiform sector of outer rainbands (Moon and Nolan, 2010; Donaher et al., 2013; Yu and Didlake, 2019). Figure 13 shows the presence of peak low-level tangential wind, particularly in UPSH, which is located between $z = 1$ and 2 km. In LOSH, the mean tangential wind in the outer rainband stratiform sector persistently decreases from the height of the low-level jet to approximately $z = 15$ km, with a subtle increase above (Figs. 13a–c). By contrast, the mean tangential velocity in SD-, CCS-, and ACS-UPSH diminishes with increasing height from the altitude of the low-level jet (Figs. 13d–f), even becoming anticyclonic above $z = 15$ km.

Moon and Nolan (2010) and Yu and Didlake (2019) demonstrated that the stratiform-induced, low-level descending inflow in outer rainbands contributes to the local tangential jet through the enhanced radially inward transport of angular momentum. However, the tangential jet between $z = 1$ and 2 km (Fig. 13) mainly reflects the vortex-scale structure of tangential wind, which decreases from the jet height to the surface due to surface friction and decreases with height above the jet due to the presence of the warm core. It is noted that the low-level tangential jet in the stratiform sector in UPSH (Figs. 13d–f) is more marked than in LOSH (Figs. 13a–c). The prominent asymmetric inflow jet between $z = 1$ and 2 km in UPSH (Figs. 12d–f), possibly reinforced by the descending inflow in the stratiform sector, results in the asymmetric tangential wind peak around the same altitude (Figs. 14d–f) and contributes additionally to the presence of the tangential jet in UPSH (Figs. f). By contrast, the lower-level asymmetric inflow jet structure in the stratiform sector is less evident in LOSH (Figs. 12a–c) than in UPSH, and the asymmetric tangential wind jet is thus absent within the boundary layer in LOSH (Figs. 14a–c).

4.3. Cross-section analysis

Figures 15 and 16 depict the radius–vertical cross sections of several variables azimuthally averaged in SD in the stratiform sector of the outer rainbands in LOSH and UPSH, respectively. In addition, the quantities in Fig. 15 are temporally averaged between 6 and 7 h, and those in Fig. 16 are temporally averaged between 35 and 36 h. Note that the radius values on the abscissae in Figs. 15 and 16 are normalized by the RMW.

We first examine the diabatic heating associated with SD, which shows the height of the heating core increasing with increasing radius, with cooling underneath the heating (Figs. 15a and 16a). This diabatic heating structure is consistent with the modified diabatic heating distribution in the idealized experiment in Yu and Didlake (2019). In particular, the heating core of SD is higher in UPSH (Fig. 16a) than in LOSH (Fig. 15a). For instance, the heating core of SD is between five and six times the RMW in UPSH and is located between $z = 7$ and 10 km (Fig. 16a), compared with that situated between $z = 5$ and 8 km in LOSH (Fig. 15a). The greater depositional growth of graupel in upper layers discussed above is likely responsible for the existence at higher altitude of the heating core in SD-UPSH.

Accompanying the diabatic heating in SD, significant outflow occurs around $z = 6.5$ km on the radially inward side of the heating core in LOSH (Fig. 15b), seemingly coincident with the result in Yu and Didlake (2019). Note that the magnitude of midlevel outflow triggered by the stratiform diabatic heating is approximately $2\text{--}3\text{ m s}^{-1}$ in Yu and Didlake (2019). Figure 15b suggests that the midlevel outflow in SD-LOSH is approximately 7 m s^{-1} , much larger than that in Yu and Didlake (2019), because of the additional asymmetric outflow forced by the VWS. Ascending outflow exists on the radially outward side of the heating core, starting near $z = 8$ km (Fig. 15b). In SD-UPSH, there are two strips of outflow on the radially inward side of the heating core, with one near $z = 5$ km and the other located at about $z = 9$ km (Fig. 16b). The former is likely associated with the heating core between four and five times the RMW, and the latter corresponds to the heating core between five and six times the RMW (Fig. 16a). Meanwhile, weak inflow exists near $z = 5$ km on the radially outward side of the heating core in SD-UPSH (Fig. 16b), agreeing with the result in Yu and Didlake (2019). Very weak inflow arises between $z = 10$ and 12 km on the radially inward side of the heating core in SD-LOSH (Fig. 15b). Although no inflow occurs above $z = 11$ km in UPSH due to the presence of VWS, the radially outward velocity at those levels is weaker on the inward side of the heating core than that on the outward side of the heating core (Fig. 16b). This increasing outflow with increasing radii above $z = 11$ km also evidences, to some degree, the occurrence of inflow forced on the inward side of the heating core between $z = 7$ and 10 km in UPSH (Fig. 16a). Many prior studies have pointed out the existence of descending inflow typically from the midtroposphere of the stratiform sector of outer rainbands, which is evident in both LOSH and UPSH, particularly at large radii (Figs. 15b and 16b).

The intense inflow within the boundary layer leads to a tangential jet (Figs. 15c and 16c) by radially inward transport of angular momentum, but it is difficult to evaluate quantitatively how much the descending inflow in SD contributes to the occurrence of the jet based on the current simulations. Note that there is an enhancement of tangential wind between four and five times the RMW above $z = 10$ km in LOSH (Fig. 15c), which is a result of the upper-level inflow associated with the heating mentioned above. In UPSH, there is also strengthened tangential velocity between $z = 10$ and 12 km (Fig. 16c), resulting from the vertical advection by amplified upward motion (Fig. 16b) related to the enhanced heating in SD (Fig. 16a).

The cross-section distributions of divergence in SD are similar in LOSH and UPSH (Figs. 15d and 16d). In general, divergence occurs in the boundary layer, with relatively higher divergence values and a deeper divergent layer at larger radii because of the subsidence approaching the surface. The confluent layer atop the boundary-layer divergence tends to become deeper with increasing radii (Figs. 15d and 16d). At upper levels (e.g., above $z = 11$ km), enhanced divergence associated with more significant outflow arises, particu-

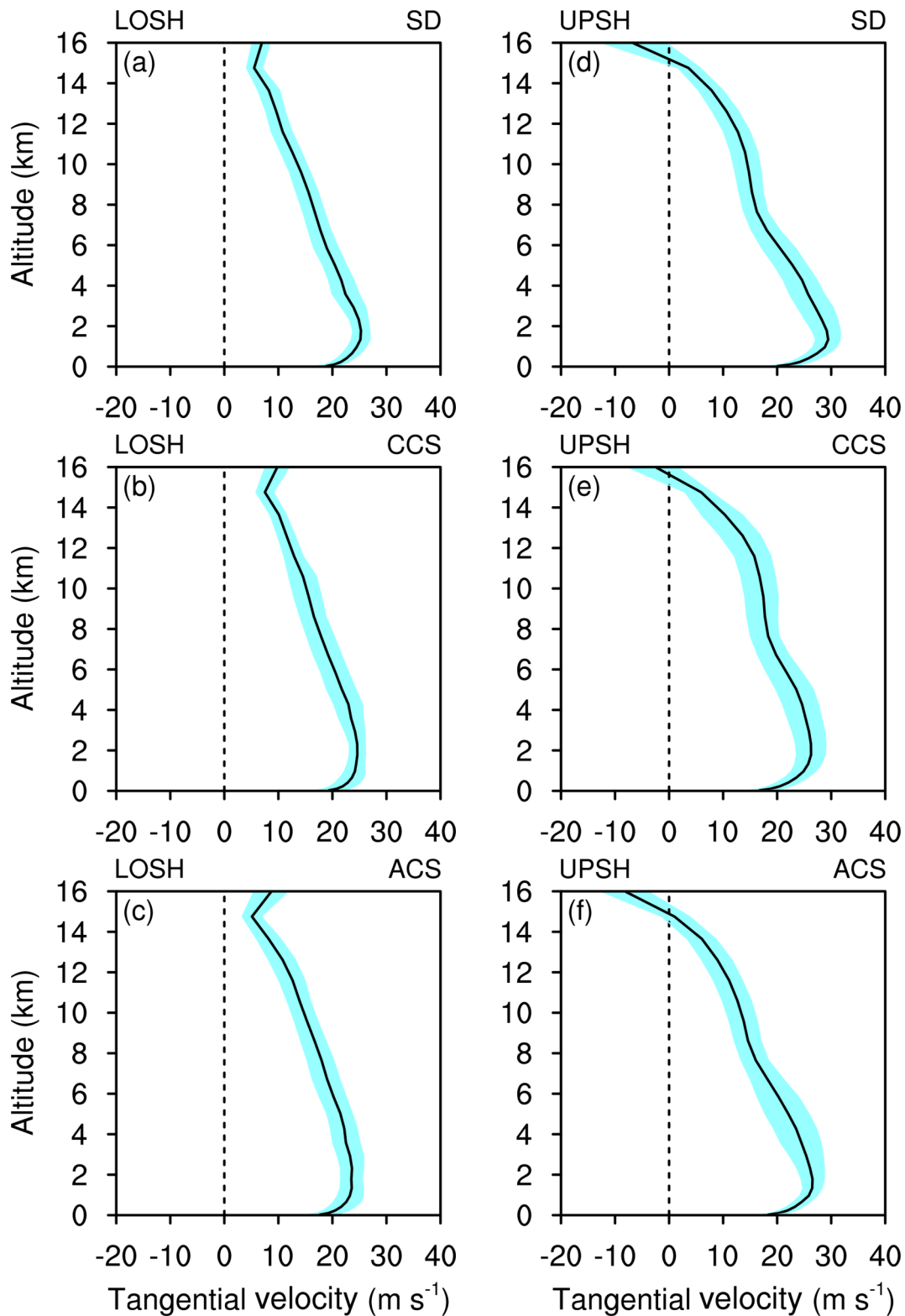


Fig. 13. As in Fig. 10, but for tangential velocity.

larly at larger radii.

The entropy distribution in SD-LOSH resembles that in UPSH (Figs. 15e and 16e). Large- θ_e is present near the surface due to high surface fluxes. For the θ_e immediately above the near-surface, the high-entropy layer decreases with height through $z = 4$ km in LOSH (Fig. 15e) and $z =$

2 km in UPSH (Fig. 16e), above which the θ_e value increases with height. The low entropy in lower layers results from significant cooling of stratiform precipitation (Figs. 15a and 16a). Interestingly, the low-level θ_e value is lower in SD-LOSH than that in UPSH (Figs. 15e and 16e), particularly beyond five times the RMW. There are more convective

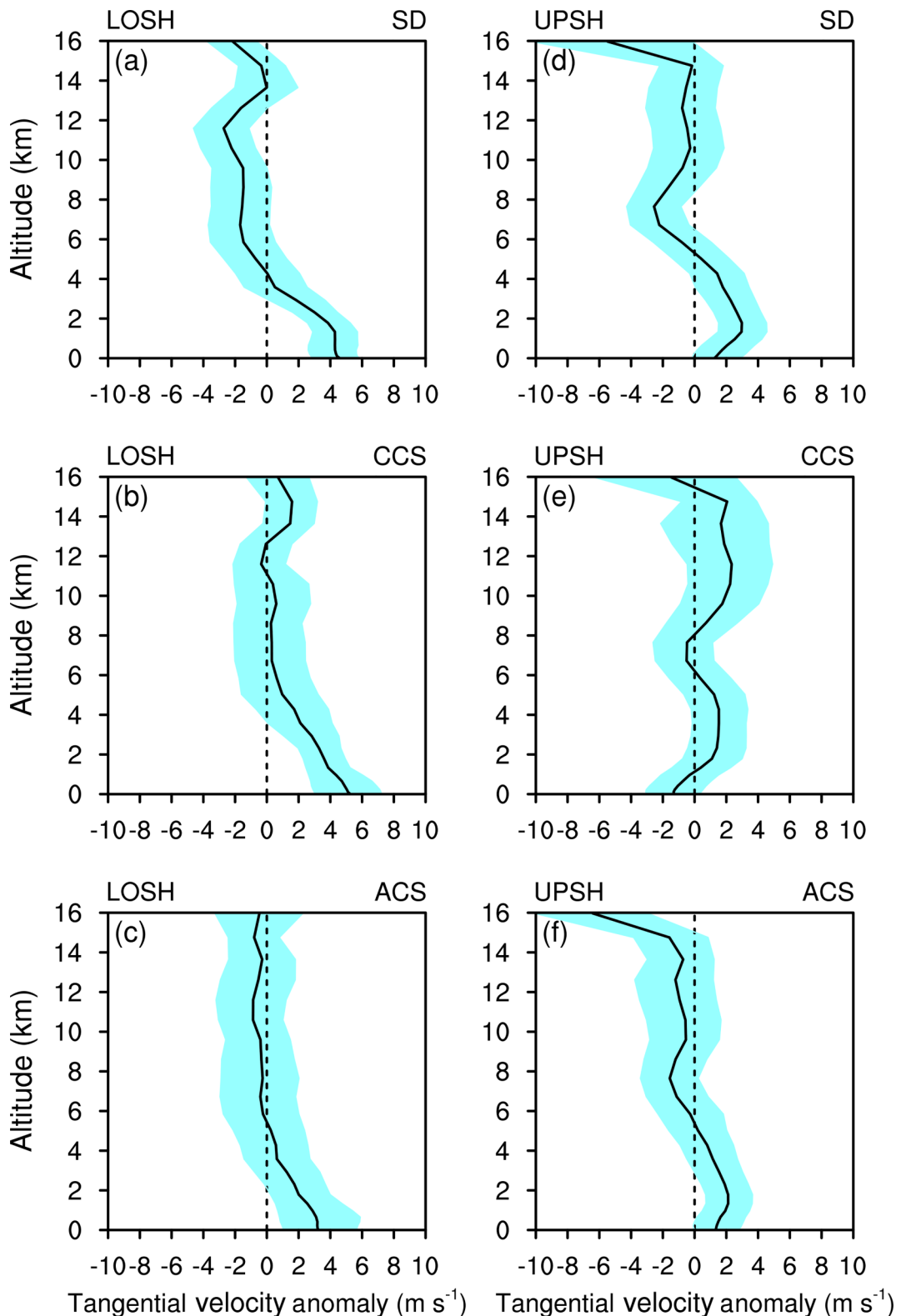


Fig. 14. As in Fig. 10, but for asymmetric tangential velocity.

grids in SD-LOSH during 6–7 h than in UPSH during 35–36 h (not shown), and the heating rate in LOSH is thereby larger than that in UPSH, particularly beyond five times the RMW (Figs. 15a and 16a). More convection embedded in SD-LOSH leads to more precipitation and more signi-

ficant evaporation at low levels (not shown). As a result, the cooling in the lower troposphere is larger in SD-LOSH during 6–7 h (Fig. 15a) than in UPSH during 35–36 h (Fig. 16a). Compared to UPSH, lower low-level entropy hence exists in SD-LOSH, particularly beyond five times the RMW

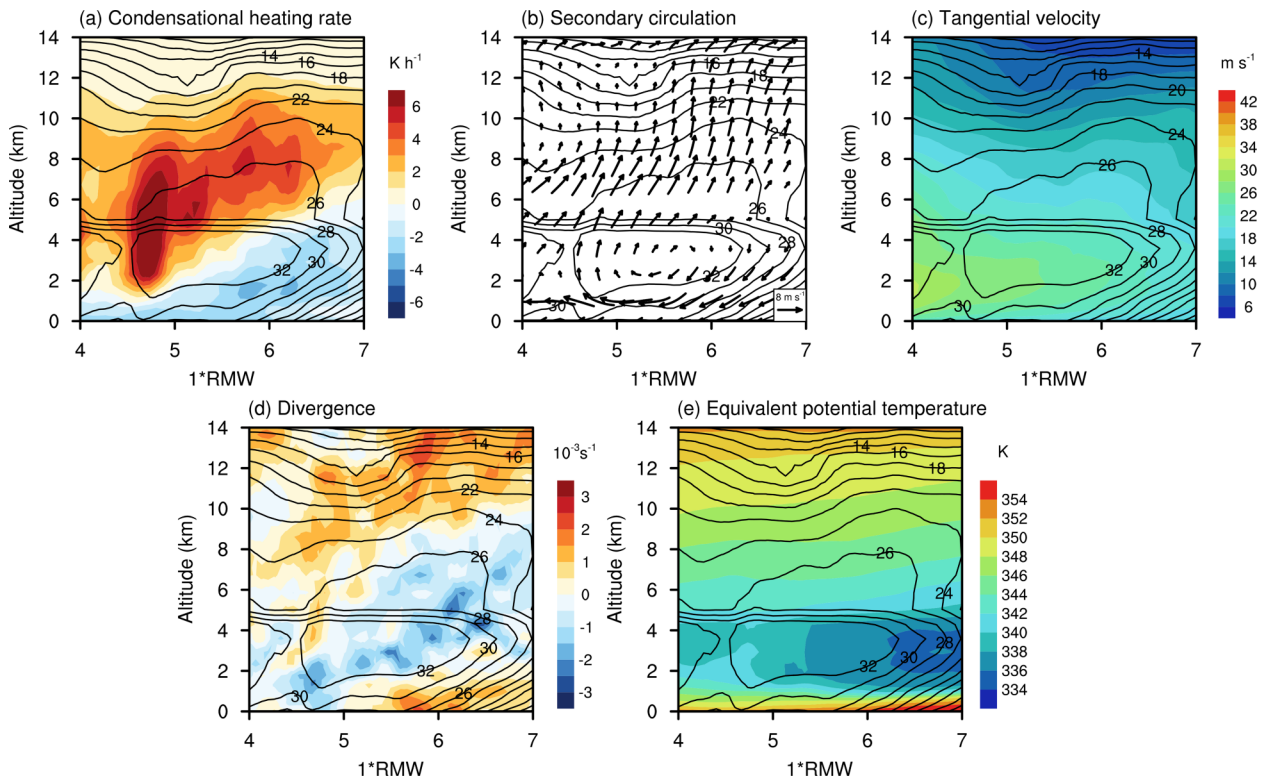


Fig. 15. Azimuthally averaged (a) condensational heating rate (shading), (b) secondary circulation (vectors), (c) tangential velocity (shading), (d) divergence (shading), and (e) equivalent potential temperature (shading) in SD-LOSH. Contours are the averaged reflectivity (units: dBZ). Note that the vertical velocity in (b) is multiplied by a factor of 10. All data shown are temporally averaged from 6 to 7 h.

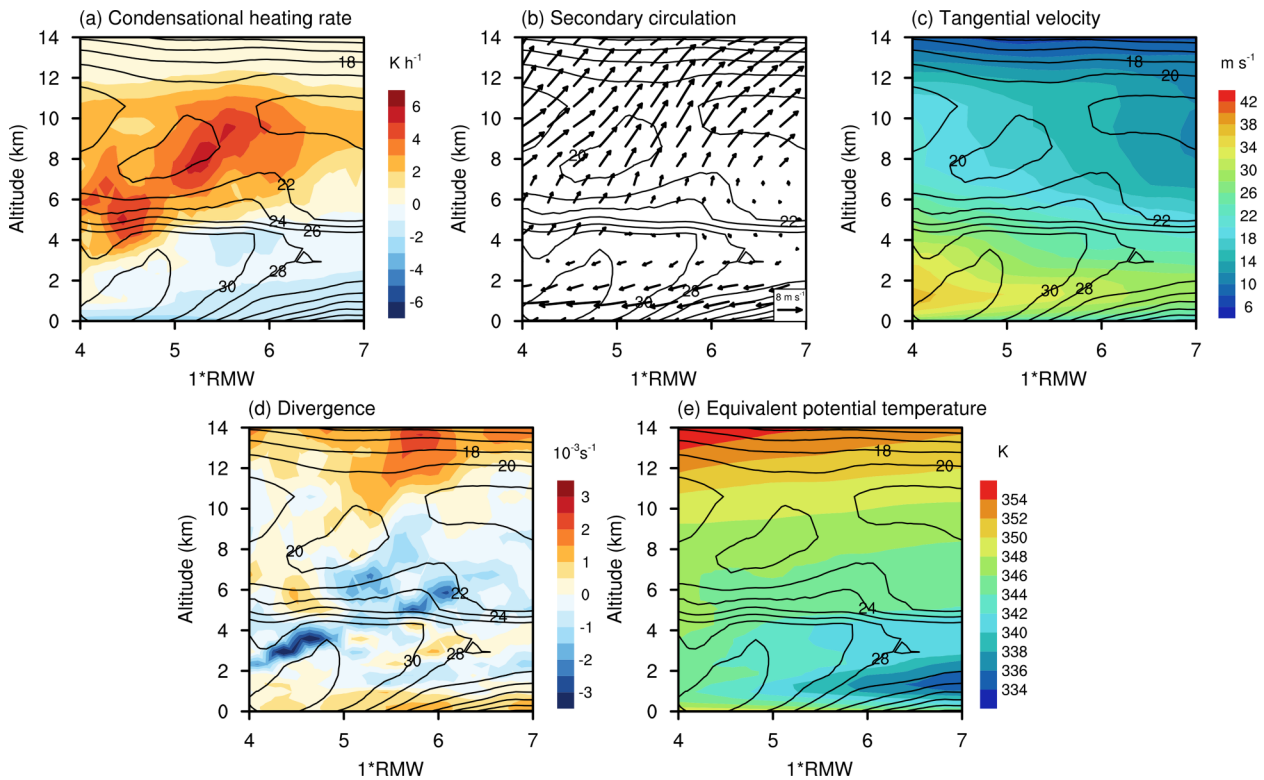


Fig. 16. As in Fig. 15, but for SD-UPSH. All data shown are temporally averaged from 35 to 36 h.

(Figs. 15e and 16e).

5. Summary

Many previous studies have indicated that vertically varying environmental flows have distinct impacts on TC structure and intensity change. In this modeling study, we examine the characteristics of the stratiform sector in outer rainbands of TCs simulated in experiments with lower-layer and upper-layer VWS, which are named LOSH and UPSH, respectively. Specifically, the stratiform sector is classified into three groupings; namely, the SD (stratiform-dominant) part, the CCS (convection-concomitant stratiform) part, and the ACS (anvil-concomitant stratiform) part. The features in SD, CCS, and ACS are elaborated.

Several characteristic resemblances of the outer rainband stratiform sector are found in LOSH and UPSH; they include:

- The stratiform sector is regularly located on the left side of the VWS vector in both experiments. The VWS tends to produce outer rainbands in the downshear quadrant, and the stratiform sector tends to be in the downwind part of the outer rainbands and thus on the left-of-shear side.
- A bright band is evident in the stratiform sector near $z = 5$ km, as observed in many previous studies. The highest reflectivity is seen in CCS, and rainwater is mainly contributive to the precipitation below the midtroposphere.
- A divergence–convergence–divergence vertical structure is present in SD and ACS in the two experiments. There is significant descending inflow starting from the midtroposphere, particularly at large radii.
- Low entropy occurs in the lower layers in SD, resulting from the significant evaporative cooling of stratiform precipitation.

In addition, significant differences in the stratiform sector structures exist in LOSH and UPSH. They are summarized below:

- The outer rainband stratiform precipitation in LOSH is less significant or less organized than in UPSH, likely because the outer rainbands simulated in LOSH are less active than in UPSH. The clouds in the stratiform sector of outer rainbands in LOSH do not display a typical CCS–SD–ACS feature.
- Reflectivity of < 20 dBZ is present at heights of 5.5–11 km in SD, CCS, and ACS in UPSH, resulting from more generation of graupel and cloud ice due to the downshear-left moister air caused by the stronger shear-forced asymmetric outflow at upper levels in UPSH.
- Deeper descending inflow in lower layers and thus a deeper near-surface divergence layer and more and stronger upward motions at upper levels appear in SD-UPSH. Particularly in SD and CCS, the lower-level asymmetric inflow jet is more visible in UPSH

than in LOSH. The upward velocity and positive mass transport between $z = 8$ and 10 km in CCS-UPSH are greater than those in CCS-LOSH, suggestive of higher diabatic heating from the deposition of graupel in UPSH. Unlike in LOSH, induced outflow rather than inflow occurs on the radially inward side of the heating core at upper levels in UPSH, due to stronger asymmetric outflow forced by the VWS.

- The low-level tangential jet in the stratiform sector in UPSH is more marked than in LOSH. Above $z = 15$ km, a subtle increase of mean tangential velocity in the stratiform sector is observed in LOSH. However, the mean tangential velocity in UPSH persistently diminishes with increasing height from the altitude of the low-level jet, and finally becomes anticyclonic above $z = 15$ km. There is an enhancement of tangential wind between four and five times the RMW above $z = 10$ km in SD-LOSH, resulting from the upper-level inflow. There is also strengthened tangential velocity between $z = 10$ and 12 km in SD-UPSH, but caused by the vertical advection by amplified upward motion.

The traits of the stratiform sector of outer rainbands in TCs in lower-layer and upper-layer VWS are investigated in this study based on the results of the idealized numerical simulations. Observations are required to validate the findings noted above. In addition, some important aspects with respect to the behavior of the outer rainband stratiform sector and associated TC structure and intensity change have not been addressed. For example, if the environmental thermodynamic patterns surrounding the TC are changed, how do the structures of the outer rainband stratiform sector vary? What are the responses of TC structure and intensity change to the interaction between the vortex-scale, VWS-forced asymmetric flow and the mesoscale stratiform-induced flow? These issues are worthy of further investigation in the future.

Acknowledgements. This work was jointly supported by the National Key Research and Development Program of China (Grant No. 2017YFC1501601), the Key Program of the Ministry of Science and Technology of China (Grant No. 2017YFE0107700), and the National Natural Science Foundation of China (Grant Nos. 41875054, 41730961, 41730960, and 41775065).

REFERENCES

- Atlas, D., K. R. Hardy, R. Wexler, and R. J. Boucher, 1963: On the origin of hurricane spiral bands. *Geofis. Int.*, **3**, 123–132.
- Barnes, G. M., E. J. Zipser, D. Jorgensen, and F. Marks, 1983: Mesoscale and convective structure of a hurricane rainband. *J. Atmos. Sci.*, **40**, 2125–2137, [https://doi.org/10.1175/1520-0469\(1983\)040<2125:MACSOA>2.0.CO;2](https://doi.org/10.1175/1520-0469(1983)040<2125:MACSOA>2.0.CO;2).
- Barnes, G. M., J. F. Gamache, M. A. LeMone, and G. J. Stossmeister, 1991: A convective cell in a hurricane rainband. *Mon. Wea. Rev.*, **119**, 776–794, [https://doi.org/10.1175/1520-0493\(1991\)119<0776:ACCIAH>2.0.CO;2](https://doi.org/10.1175/1520-0493(1991)119<0776:ACCIAH>2.0.CO;2).
- Bender, M. A., 1997: The effect of relative flow on the asymmetric structure in the interior of hurricanes. *J. Atmos. Sci.*, **54**,

- 703–724, [https://doi.org/10.1175/1520-0469\(1997\)054<0703:TEORFO>2.0.CO;2](https://doi.org/10.1175/1520-0469(1997)054<0703:TEORFO>2.0.CO;2).
- Braun, S. A., and L. G. Wu, 2007: A numerical study of Hurricane Erin (2001). Part II: Shear and the organization of eyewall vertical motion. *Mon. Wea. Rev.*, **135**, 1179–1194, <https://doi.org/10.1175/MWR3336.1>.
- Braun, S. A., M. T. Montgomery, and Z. Pu, 2006: High-resolution simulation of Hurricane Bonnie (1998). Part I: The organization of eyewall vertical motion. *J. Atmos. Sci.*, **63**, 19–42, <https://doi.org/10.1175/JAS3598.1>.
- Chen, G., C.-C. Wu, and Y.-H. Huang, 2018: The role of near-core convective and stratiform heating/cooling in tropical cyclone structure and intensity. *J. Atmos. Sci.*, **75**, 297–326, <https://doi.org/10.1175/JAS-D-17-0122.1>.
- Corbosiero, K. L., and J. Molinari, 2003: The relationship between storm motion, vertical wind shear, and convective asymmetries in tropical cyclones. *J. Atmos. Sci.*, **60**, 366–376, [https://doi.org/10.1175/1520-0469\(2003\)060<0366:TRBSMV>2.0.CO;2](https://doi.org/10.1175/1520-0469(2003)060<0366:TRBSMV>2.0.CO;2).
- DeMaria, M., 1996: The effect of vertical shear on tropical cyclone intensity change. *J. Atmos. Sci.*, **53**, 2076–2088, [https://doi.org/10.1175/1520-0469\(1996\)053<2076:TEOVSO>2.0.CO;2](https://doi.org/10.1175/1520-0469(1996)053<2076:TEOVSO>2.0.CO;2).
- Didlake, A. C., and R. A. Houze, 2013: Dynamics of the stratiform sector of a tropical cyclone rainband. *J. Atmos. Sci.*, **70**, 1891–1911, <https://doi.org/10.1175/jas-d-12-0245.1>.
- Didlake, A. C., P. D. Reasor, R. F. Rogers, and W.-C. Lee, 2018: Dynamics of the transition from spiral rainbands to a secondary eyewall in Hurricane Earl (2010). *J. Atmos. Sci.*, **75**, 2909–2929, <https://doi.org/10.1175/JAS-D-17-0348.1>.
- Donaher, S. L., B. A. Albrecht, M. Fang, and W. Brown, 2013: Wind profiles in tropical cyclone stratiform rainbands over land. *Mon. Wea. Rev.*, **141**, 3933–3949, <https://doi.org/10.1175/MWR-D-13-00081.1>.
- Dunion, J. P., 2011: Rewriting the climatology of the tropical North Atlantic and Caribbean Sea atmosphere. *J. Climate*, **24**, 893–908, <https://doi.org/10.1175/2010JCLI3496.1>.
- Finocchio, P. M., and S. J. Majumdar, 2017: A statistical perspective on wind profiles and vertical wind shear in tropical cyclone environments of the northern hemisphere. *Mon. Wea. Rev.*, **145**, 361–378, <https://doi.org/10.1175/MWR-D-16-0221.1>.
- Finocchio, P. M., S. J. Majumdar, D. S. Nolan, and M. Iskandarani, 2016: Idealized tropical cyclone responses to the height and depth of environmental vertical wind shear. *Mon. Wea. Rev.*, **144**, 2155–2175, <https://doi.org/10.1175/MWR-D-15-0320.1>.
- Frank, W. M., and E. A. Ritchie, 1999: Effects of environmental flow upon tropical cyclone structure. *Mon. Wea. Rev.*, **127**, 2044–2061, [https://doi.org/10.1175/1520-0493\(1999\)127<2044:EOEFUT>2.0.CO;2](https://doi.org/10.1175/1520-0493(1999)127<2044:EOEFUT>2.0.CO;2).
- Frank, W. M., and E. A. Ritchie, 2001: Effects of vertical wind shear on the intensity and structure of numerically simulated hurricanes. *Mon. Wea. Rev.*, **129**, 2249–2269, [https://doi.org/10.1175/1520-0493\(2001\)129<2249:EOVWSO>2.0.CO;2](https://doi.org/10.1175/1520-0493(2001)129<2249:EOVWSO>2.0.CO;2).
- Franklin, C. N., G. J. Holland, and P. T. May, 2006: Mechanisms for the generation of mesoscale vorticity features in tropical cyclone rainbands. *Mon. Wea. Rev.*, **134**, 2649–2669, <https://doi.org/10.1175/MWR3222.1>.
- Franklin, J. L., S. J. Lord, S. E. Feuer, and F. D. Marks, 1993: The kinematic structure of Hurricane Gloria (1985) determined from nested analyses of dropwindsonde and doppler radar data. *Mon. Wea. Rev.*, **121**, 2433–2451, [https://doi.org/10.1175/1520-0493\(1993\)121<2433:TKSOHG>2.0.CO;2](https://doi.org/10.1175/1520-0493(1993)121<2433:TKSOHG>2.0.CO;2).
- Fu, H., Y. Q. Wang, M. Riemer, and Q. Q. Li, 2019: Effect of unidirectional vertical wind shear on tropical cyclone intensity change—Lower-layer shear versus upper - layer shear. *J. Geophys. Res.*, **124**, 6265–6282, <https://doi.org/10.1029/2019JD030586>.
- Gu, J.-F., Z.-M. Tan, and X. Qiu, 2016: Quadrant-dependent evolution of low-level tangential wind of a tropical cyclone in the shear flow. *J. Atmos. Sci.*, **73**, 1159–1177, <https://doi.org/10.1175/JAS-D-15-0165.1>.
- Hazelton, A. T., R. Rogers, and R. E. Hart, 2015: Shear-relative asymmetries in tropical cyclone eyewall slope. *Mon. Wea. Rev.*, **143**, 883–903, <https://doi.org/10.1175/MWR-D-14-0122.1>.
- Hence, D. A., and R. A. Houze, 2008: Kinematic structure of convective-scale elements in the rainbands of Hurricanes Katrina and Rita (2005). *J. Geophys. Res.*, **113**, <https://doi.org/10.1029/2007JD009429>.
- Hendricks, E. A., M. S. Peng, B. Fu, and T. Li, 2010: Quantifying environmental control on tropical cyclone intensity change. *Mon. Wea. Rev.*, **138**, 3243–3271, <https://doi.org/10.1175/2010MWR3185.1>.
- Heysmsfield, G. M., J. Simpson, J. Halverson, L. Tian, E. Ritchie, and J. Molinari, 2006: Structure of highly sheared tropical storm Chantal during CAMEX-4. *J. Atmos. Sci.*, **63**, 268–287, <https://doi.org/10.1175/JAS3602.1>.
- Houze, R. A., 1997: Stratiform precipitation in regions of convection: A meteorological paradox? *Bull. Amer. Meteor. Soc.*, **78**, 2179–2196, [https://doi.org/10.1175/1520-0477\(1997\)078<2179:SPIROC>2.0.CO;2](https://doi.org/10.1175/1520-0477(1997)078<2179:SPIROC>2.0.CO;2).
- Houze, R. A., 2010: Clouds in tropical cyclones. *Mon. Wea. Rev.*, **138**, 293–344, <https://doi.org/10.1175/2009MWR2989.1>.
- Li, Q. Q., and Q. X. Fang, 2018: A numerical study of convective-scale structures in the outer cores of sheared tropical cyclones. Part I: Updraft traits in different vertical wind shear magnitudes. *J. Geophys. Res.*, **123**, 12097–12116, <https://doi.org/10.1029/2018JD029022>.
- Li, Q. Q., Y. H. Duan, H. Yu, and G. Fu, 2008: A high-resolution simulation of Typhoon Ranim (2004) with MM5. Part I: Model verification, inner-core shear, and asymmetric convection. *Mon. Wea. Rev.*, **136**, 2488–2506, <https://doi.org/10.1175/2007MWR2159.1>.
- Li, Q. Q., Y. Q. Wang, and Y. H. Duan, 2017: A numerical study of outer rainband formation in a sheared tropical cyclone. *J. Atmos. Sci.*, **74**, 203–227, <https://doi.org/10.1175/JAS-D-16-0123.1>.
- Li, Q. Q., and Y. Q. Wang, 2012: A comparison of inner and outer spiral rainbands in a numerically simulated tropical cyclone. *Mon. Wea. Rev.*, **140**, 2782–2805, <https://doi.org/10.1175/MWR-D-11-00237.1>.
- Marks, F. D., 1985: Evolution of the structure of precipitation in Hurricane Allen (1980). *Mon. Wea. Rev.*, **113**, 909–930, [https://doi.org/10.1175/1520-0493\(1985\)113<0909:eotsop>2.0.co;2](https://doi.org/10.1175/1520-0493(1985)113<0909:eotsop>2.0.co;2).
- Marks, F. D., 2003: State of the science: radar view of tropical cyclones. *Amer. Meteor. Soc.*, **30**, https://doi.org/10.1007/978-1-878220-36-3_3.
- Marks, F. D., R. A. Houze, and J. F. Gamache, 1992: Dual-Aircraft investigation of the inner core of Hurricane Norbert. Part I: Kinematic structure. *J. Atmos. Sci.*, **49**, 919–942, [https://doi.org/10.1175/1520-0469\(1992\)049<0919:daioti>2.0.co;2](https://doi.org/10.1175/1520-0469(1992)049<0919:daioti>2.0.co;2).
- May, P. T., and G. J. Holland, 1999: The role of potential vorticity generation in tropical cyclone rainbands. *J. Atmos. Sci.*,

- 56, 1224–1228, [https://doi.org/10.1175/1520-0469\(1999\)056<1224:TROPVG>2.0.CO;2](https://doi.org/10.1175/1520-0469(1999)056<1224:TROPVG>2.0.CO;2).
- Moon, Y., and D. S. Nolan, 2010: The dynamic response of the hurricane wind field to spiral rainband heating. *J. Atmos. Sci.*, **67**, 1779–1805, <https://doi.org/10.1175/2010JAS3171.1>.
- Onderlinde, M. J., and D. S. Nolan, 2014: Environmental helicity and its effects on development and intensification of tropical cyclones. *J. Atmos. Sci.*, **71**, 4308–4320, <https://doi.org/10.1175/JAS-D-14-0085.1>.
- Paterson, L. A., B. N. Hanstrum, N. E. Davidson, and H. C. Weber, 2005: Influence of environmental vertical wind shear on the intensity of hurricane-strength tropical cyclones in the Australian region. *Mon. Wea. Rev.*, **133**, 3644–3660, <https://doi.org/10.1175/MWR3041.1>.
- Qiu, X., and Z.-M. Tan, 2013: The roles of asymmetric inflow forcing induced by outer rainbands in tropical cyclone secondary eyewall formation. *J. Atmos. Sci.*, **70**, 953–974, <https://doi.org/10.1175/JAS-D-12-084.1>.
- Reasor, P. D., M. T. Montgomery, and L. D. Grasso, 2004: A new look at the problem of tropical cyclones in vertical shear flow: Vortex resiliency. *J. Atmos. Sci.*, **61**, 3–22, [https://doi.org/10.1175/1520-0469\(2004\)061<0003:ANLATP>2.0.CO;2](https://doi.org/10.1175/1520-0469(2004)061<0003:ANLATP>2.0.CO;2).
- Reasor, P. D., R. Rogers, and S. Lorsolo, 2013: Environmental flow impacts on tropical cyclone structure diagnosed from airborne doppler radar composites. *Mon. Wea. Rev.*, **141**, 2949–2969, <https://doi.org/10.1175/MWR-D-12-00334.1>.
- Riemer, M., M. T. Montgomery, and M. E. Nicholls, 2010: A new paradigm for intensity modification of tropical cyclones: thermodynamic impact of vertical wind shear on the inflow layer. *Atmos. Chem. Phys.*, **10**, 3163–3188, <https://doi.org/10.5194/acp-10-3163-2010>.
- Rios-Berrios, R., and R. D. Torn, 2017: Climatological analysis of tropical cyclone intensity changes under moderate vertical wind shear. *Mon. Wea. Rev.*, **145**, 1717–1738, <https://doi.org/10.1175/MWR-D-16-0350.1>.
- Rogers, R., 2010: Convective-scale structure and evolution during a high-resolution simulation of tropical cyclone rapid intensification. *J. Atmos. Sci.*, **67**, 44–70, <https://doi.org/10.1175/2009JAS3122.1>.
- Rotunno, R., J. B. Klemp, and M. L. Weisman, 1988: A theory for strong, long-lived squall lines. *J. Atmos. Sci.*, **45**, 463–485, [https://doi.org/10.1175/1520-0469\(1988\)045<0463:ATFSL>2.0.CO;2](https://doi.org/10.1175/1520-0469(1988)045<0463:ATFSL>2.0.CO;2).
- Rozoff, C. M., W. H. Schubert, B. D. McNoldy, and J. P. Kossin, 2006: Rapid filamentation zones in intense tropical cyclones. *J. Atmos. Sci.*, **63**, 325–340, <https://doi.org/10.1175/jas3595.1>.
- Shu, S. J., Y. Wang, and L. L. Bai, 2013: Insight into the role of lower-layer vertical wind shear in tropical cyclone intensification over the western North Pacific. *Acta Meteorol. Sin.*, **27**, 356–363, <https://doi.org/10.1007/s13351-013-0310-9>.
- Tang, B., and K. Emanuel, 2010: Midlevel ventilation's constraint on tropical cyclone intensity. *J. Atmos. Sci.*, **67**, 1817–1830, <https://doi.org/10.1175/2010JAS3318.1>.
- Tang, B., and K. Emanuel, 2012: Sensitivity of tropical cyclone intensity to ventilation in an axisymmetric model. *J. Atmos. Sci.*, **69**, 2394–2413, <https://doi.org/10.1175/JAS-D-11-0232.1>.
- Uhlhorn, E. W., B. W. Klotz, T. Vukicevic, P. D. Reasor, and R. F. Rogers, 2014: Observed hurricane wind speed asymmetries and relationships to motion and environmental shear. *Mon. Wea. Rev.*, **142**, 1290–1311, <https://doi.org/10.1175/MWR-D-13-00249.1>.
- Velden, C. S., and J. Sears, 2014: Computing deep-tropospheric vertical wind shear analyses for tropical cyclone applications: Does the methodology matter? *Wea. Forecasting*, **29**, 1169–1180, <https://doi.org/10.1175/WAF-D-13-00147.1>.
- Wang, Y. Q., 2001: An explicit simulation of tropical cyclones with a triply nested movable mesh primitive equation model: TCM3. Part I: Model description and control experiment. *Mon. Wea. Rev.*, **129**, 1370–1394, [https://doi.org/10.1175/1520-0493\(2001\)129<1370:AESOTC>2.0.CO;2](https://doi.org/10.1175/1520-0493(2001)129<1370:AESOTC>2.0.CO;2).
- Wang, Y. Q., 2007: Structure and formation of an annular hurricane simulated in a fully compressible, nonhydrostatic model—TCM4*. *J. Atmos. Sci.*, **65**, 1505–1527, <https://doi.org/10.1175/2007JAS2528.1>.
- Wang, Y. Q., 2009: How do outer spiral rainbands affect tropical cyclone structure and intensity? *J. Atmos. Sci.*, **66**, 1250–1273, <https://doi.org/10.1175/2008JAS2737.1>.
- Wang, Y. Q., Y. Rao, Z.-M. Tan, and D. Schönemann, 2015: A statistical analysis of the effects of vertical wind shear on tropical cyclone intensity change over the Western North Pacific. *Mon. Wea. Rev.*, **143**, 3434–3453, <https://doi.org/10.1175/MWR-D-15-0049.1>.
- Willoughby, H. E., F. D. Marks Jr., and R. J. Feinberg, 1984: Stationary and moving convective bands in hurricanes. *J. Atmos. Sci.*, **41**, 3189–3211, [https://doi.org/10.1175/1520-0469\(1984\)041<3189:SAMCBI>2.0.CO;2](https://doi.org/10.1175/1520-0469(1984)041<3189:SAMCBI>2.0.CO;2).
- Wong, M. L. M., and J. C. L. Chan, 2004: Tropical cyclone intensity in vertical wind shear. *J. Atmos. Sci.*, **61**, 1859–1876, [https://doi.org/10.1175/1520-0469\(2004\)061<1859:TCIIVW>2.0.CO;2](https://doi.org/10.1175/1520-0469(2004)061<1859:TCIIVW>2.0.CO;2).
- Wu, L. G., S. A. Braun, J. Halverson, and G. Heymsfield, 2006: A numerical study of Hurricane Erin (2001). Part I: Model verification and storm evolution. *J. Atmos. Sci.*, **63**, 65–86, <https://doi.org/10.1175/JAS3597.1>.
- Xu, Y. M., and Y. Q. Wang, 2013: On the initial development of asymmetric vertical motion and horizontal relative flow in a mature tropical cyclone embedded in environmental vertical shear. *J. Atmos. Sci.*, **70**, 3471–3491, <https://doi.org/10.1175/JAS-D-12-0335.1>.
- Yu, C.-L., and A. C. Didlake, 2019: Impact of stratiform rainband heating on the tropical cyclone wind field in idealized simulations. *J. Atmos. Sci.*, **76**, 2443–2462, <https://doi.org/10.1175/JAS-D-18-0335.1>.
- Yu, C.-K., C.-Y. Lin, L.-W. Cheng, J.-S. Luo, C.-C. Wu, and Y. Chen, 2018: The degree of prevalence of similarity between outer tropical cyclone rainbands and squall lines. *Sci. Rep.*, **8**, <https://doi.org/10.1038/s41598-018-26553-8>.
- Yuter, S. E., and R. A. Houze, 1995a: Three-dimensional kinematic and microphysical evolution of Florida cumulonimbus. Part II: Frequency distributions of vertical velocity, reflectivity, and differential reflectivity. *Mon. Wea. Rev.*, **123**, 1941–1963, [https://doi.org/10.1175/1520-0493\(1995\)123<1941:TDKAME>2.0.CO;2](https://doi.org/10.1175/1520-0493(1995)123<1941:TDKAME>2.0.CO;2).
- Yuter, S. E., and R. A. Houze, 1995b: Three-dimensional kinematic and microphysical evolution of Florida cumulonimbus. Part III: Vertical Mass Transport, Mass Divergence, and Synthesis. *Mon. Wea. Rev.*, **123**, 1964–1983, [https://doi.org/10.1175/1520-0493\(1995\)123<1964:TDKAME>2.0.CO;2](https://doi.org/10.1175/1520-0493(1995)123<1964:TDKAME>2.0.CO;2).
- Zeng, Z. H., Y. Q. Wang, and L. S. Chen, 2010: A statistical analysis of vertical shear effect on tropical cyclone intensity change in the North Atlantic. *Geophys. Res. Lett.*, **37**, L02802, <https://doi.org/10.1029/2009GL041788>.